Chem Soc Rev

# Topochemical Synthesis of 2D Materials



| | |
|---|---|
| Journal: | *Chemical Society Reviews* |
| Manuscript ID | CS-REV-08-2018-000649.R1 |
| Article Type: | Review Article |
| Date Submitted by the Author: | 02-Oct-2018 |
| Complete List of Authors: | Xiao, Xu; Drexel University, and Department of Materials Science and Engineering<br>Wang, Hao; Soochow University, Department of Energy<br>Urbankowski, Patrick ; A.J. Drexel Nanomaterials Institute, and Materials Science and Engineering Department, Drexel University<br>Gogotsi, Yury; A.J. Drexel Nanomaterials Institute, and Materials Science and Engineering Department, Drexel University, |
| | |

# Topochemical Synthesis of 2D Materials

Xu Xiao[†], Hao Wang[†], Patrick Urbankowski[†], Yury Gogotsi*

Department of Materials Science and Engineering and A. J. Drexel Nanomaterials Institute, Drexel University, Philadelphia, Pennsylvania 19104, USA

[†] These authors contributed equally.

* Corresponding author. E-mail: gogotsi@drexel.edu

**Abstract:** Since the demonstration of the unique properties of single-layer graphene and transition metal dichalcogenides (TMDs), research on two-dimensional (2D) materials has become one of the hottest topics, with the family of 2D materials quickly expanding. This expansion is mainly attributable to the development of new synthesis methods to create new materials. This review will summarize and critically analyze topochemical synthesis methods for synthesizing novel 2D materials. For example, the emerging family of 2D transition metal carbides, nitrides and carbonitrides (MXenes) are synthesized primarily by selective etching of "A" (metal) elements from MAX phases. Another 2D material, hydrogenated germanene is produced by selective etching of calcium digermanide ($CaGe_2$). The topochemical transformation of one dichalcogenide into another and 2D oxides into 2D carbides or nitrides have attracted great attention because materials with many useful and diverse properties can be obtained by these methods. Topochemical synthesis methods provide alternative ways of synthesizing 2D materials not requiring van der Waals bonded solid precursors or vapor phase deposition, but they have not been comprehensively reviewed. In this review, we describe common principles of topochemical synthesis of 2D materials, explain synthesis mechanisms and offer an outlook for future research.

## 1. INTRODUCTION

The discovery of graphene demonstrated that materials can manifest distinctive properties, when they adapt a two-dimensional (2D) atomically thin structure.[1] This demonstration opened a new door for materials research and extensive studies of the synthesis of 2D materials offered an opportunity for fast expansion of this family of materials.[2, 3] In general, there are some restrictions on conventional synthesis methods because 2D materials are metastable and non-equilibrium processes are applied to their synthesis. Gas-phase synthesis, including chemical or

physical vapor deposition (CVD or PVD) can produce high-quality 2D materials of large lateral size on substrates, however the yield of material from CVD or PVD synthesis may be sufficient for electronic devices, but is not high enough for many other applications, including energy storage.[4, 5] Solution-based methods such as exfoliation and chemical synthesis offer simple processing and much higher yields. However, exfoliation is only feasible for layered compounds bonded by weak van der Waals forces along one direction that can be separated by mechanical or intercalant-assisted cleavage in solution.[6] Another promising strategy is topochemical synthesis. In general, a topochemical reaction is defined as a reversible or irreversible reaction that involves the introduction of a guest species into a host structure, and that results in significant structural modifications to the host. Here, for topochemical synthesis, it can be broadly defined as adding, extracting or substituting elements to or from precursors in an environment of liquid or gas for synthesis of new materials which retain the structure or, at least, morphology of precursors.

Recently, enabled by the development of many novel synthesis methods, a variety of novel 2D materials have been reported. For instance, in 2011, a family of 2D transition metal carbides, nitrides, and carbonitrides (MXenes) have been synthesized by using selective etching, which is a kind of topochemical synthesis. These materials have a formula of $M_{n+1}X_nT_x$, where M represents a transition metal (such as Sc, Ti, Zr, Hf, V, Nb, Ta, Cr, Mo, etc.), X is carbon and/or nitrogen, and $T_x$ describes the surface terminations (e.g. O, OH, F, etc.).[7] MXenes are synthesized by the selective etching of A elements (mostly group 13 and 14 elements of the periodic table) from their parent precursors–MAX phases, where M and X refer to the same elements in MXenes.[8, 9]

A similar strategy is applied to produce hydrogen-terminated silicon and germanium nanosheets, named silicane and germanane, which are selectively etched from calcium silicide and calcium germanide, respectively.[10-20] Some 3D zeolites can also be selectively etched to form 2D zeolite.[21] This selective removal of atoms, commonly referred to as topochemical deintercalation synthesis, can largely expand the family of 2D materials by choosing suitable precursors and etchants.

Another strategy that has attracted attention recently for synthesis of novel 2D non-layered structured materials is the salt-templating method, a topochemical transformation technique that can be used for various non-layered materials, such as 2D *h*-$MoO_3$.[22] These non-layered structured materials have some unique properties. For instance, *h*-$MoO_3$ has a large internal pore

which is favorable for energy storage. However, they cannot be exfoliated into 2D morphology by exfoliation. By using salt-templating method, a precursor is transformed into a target 2D material on the surface of a salt crystal, by virtue of a lattice match. Other candidates, including transition metal dichalcogenides (TMDs) and metal carbides have also been topochemically transformed to metal nitrides.[23] This is of particular interest for fundamental studies since one can attain and compare two different materials with the same structure and stoichiometry. For instance, a topochemical transformation from carbide MXenes to nitride MXenes have directly demonstrated that nitrides have a higher electron conductivity than their carbide counterparts.[24]

In this review, we aim to summarize recent developments in the synthesis of 2D materials beyond graphene and TMDs, focusing on topochemical synthesis routes, which include topochemical deintercalation and transformation (Fig. 1). Representative methods and materials will be reviewed, followed with a detailed explanation of synthesis mechanisms. We will also give descriptions of outstanding problems and a prospective outlook on future research of topochemical synthesis of 2D materials.

## 2. SELECTIVE ETCHING AND CHEMICAL EXFOLIATION OF LAYERED SOLIDS

### 2.1. 2D transition metal carbides, nitrides and carbonitrides (MXenes)

A large family of 2D transition metal carbides, nitrides and carbonitrides, named MXenes, was introduced in 2011.[7, 25-28] Close to 30 members of the MXene family have been synthesized in three different stoichiometries ($M_2X$, $M_3X_2$, and $M_4X_3$), including double-metal MXenes ($M'_2M''C_2$ and $M'_2M''_2C_3$) and MXene with ordered divacancies (e.g. $Mo_{1.33}C$) (Fig. 2a).[29-32] Additionally, dozens more have been predicted.[33-36] The naming convention of MXenes comes from two aspects: "ene" referring to an atomically thin 2D structure similar to graphene and "MX", derived from their parent MAX phases (for example, the first MXene $Ti_3C_2T_x$ was etched from $Ti_3AlC_2$ MAX phase) by removal of "A" element.[37, 38] Generally, MXenes have a formula of $M_{n+1}X_nT_x$. Here $n+1$ M layers and $n$ X layers are alternately stacked, leaving the outermost M layers with terminations, $T_x$. This unique structure exhibits many useful properties.[39-43] For example, pursuing high conductivity with MXenes hydrophilic surfaces is of great importance for various applications, such as electrochemical energy storage.[44-47] In contrast to graphene, in which the surface becomes hydrophilic only with O-terminations, while the conductivity vastly

decreases simultaneously, high conductivity (~ 8,000 S/cm) is exhibited in hydrophilic freestanding MXene films and it reaches ~10,000 S/cm in supported thin films,[47] which have demonstrated promising performance in applications including but not limited to energy storage,[48, 49] electrocatalysis,[50, 51] water desalination,[52, 53] electromagnetic interference (EMI) shielding,[54-56] and transparent conducting films.[57-60]

### 2.1.1. Selective etching of MAX phases

Unlike graphene and TMDs, the synthesis of MXenes cannot be performed by mechanical exfoliation due to the strong metallic bonds between M and A layers. It should be noted that Ananthakumar *et al.* claimed shear-induced micromechanical synthesis of $Ti_3SiC_2$ nanosheets, which they called MAXene.[61] However, there was no direct evidence to prove this MAXene possessed single-layer or few-layer thicknesses. Selective etching of MAX phases to remove A elements is usually required to produce MXenes, because M–X bonds are much stronger than chemically active M–A bonds.[62]

In general, the etching process requires preparation of an etchant solution, mixing MAX phase with the etchant, followed by stirring for several hours at temperatures ranging from room temperature to 90 °C (Fig. 2b). After etching, the resultant powder is washed repeatedly to remove the residual etchant and salts. This step is repeated until the pH is close to neutral (commonly reported to be around pH 6). This etching produces multilayered MXene, which can be described as many layers of MXene flakes stacked together in a single particle. Multilayered MXene can be isolated from solution by vacuum filtration or other methods followed by vacuum drying. To remove the excess water, vacuum drying of $Ti_3C_2T_x$ powders is applied at 80 °C. The presence of water molecules trapped between MXene layers can be observed in the (00*l*) peaks. The multilayered MXenes with weak hydrogen bonding between the layers can be delaminated to form single- to few-layered flakes by solution processing methods and form stable colloidal solutions (Fig. 2c). A detailed protocol can be found in a recent synthesis and processing guideline for $Ti_3C_2T_x$ MXene.[37]

To date, mostly etchable MAX phases are Al-containing ones, and just very recently the first Si-containing $Ti_3SiC_2$ MAX has been successfully etched to produce $Ti_3C_2T_x$ MXene[63] by the same method that we used to selectively etch SiC whiskers in the past.[64] Widely used etchants for top-down synthesis methods include aqueous fluoride-containing acids or salts, which can be categorized into two types: aqueous hydrofluoric acid (HF) and an *in situ* HF-forming etchants,

such as metal fluoride (e.g. LiF) mixed with an acid (e.g. HCl) and ammonium hydrogen bifluoride ($NH_4HF_2$).[46, 59] For the aqueous HF method, the concentration of HF varies quite a bit in literature, especially for $Ti_3C_2T_x$ MXene. Complete removal of Al from $Ti_3AlC_2$ MAX using 3 to 50 wt.% HF has been proven from X-ray diffraction (XRD) patterns, showing absence of residual peaks of $Ti_3AlC_2$ and appearance of a (002) peak of MXene positioned around 9.5°. Notably, the etching time for different concentrations varies from 2 to 24 h. For instance, in the first paper on the synthesis of MXenes, 10 g of $Ti_3AlC_2$ powders was immersed in 100 mL of a 50% concentrated HF solution and stirred at room temperature for 2 h. When using low-concentration HF, such as 5 wt%, however, 24 h etching should be sufficient to completely etch the Al. This is very important not only for monitoring the use of hazardous HF, but also for research on the influence of HF concentration on the quality of MXenes. For example, the selective etching of MAX phases always brings various terminations on the surface of MXenes, such as −F, −O, −OH.[7] Normally, the use of a lower concentration HF for selective etching results in more O but less F (higher O/F ratio) in the produced $Ti_3C_2T_x$. In addition, MXenes etched by HF of higher concentration have more defects, which are not desirable for majority of applications. Choosing a suitable HF concentration is important for controlling MXene structure and properties.

Besides aqueous HF, etchants containing *in situ* formed HF can also be used to etch MAX phases. For example, HCl and LiF can react to form HF *in situ*, producing Li-intercalated MXene "clay".[46] In this case, $Ti_3AlC_2$ MAX powder was added to a mixture of 5 M LiF/6 M HCl and stirred at 40 °C for 45 h. The presence of protons and $F^-$ plays an important role during the etching process, and $Li^+$ intercalates into multilayered MXenes or exchanges with the surface $H^+$ on MXenes to further expand the spacing and weaken the bonding between adjacent MXene layers. This can be confirmed by larger shift of the (002) peak in XRD patterns to lower angles, indicating a greater distance between the layers. Another modified *in situ* LiF/HCl etching method is called minimally intensive layer delamination (MILD) which used 7.5 M LiF/9 M HCl instead of 5 M LiF/6 M HCl.[65] This method can generate MXene with a large lateral size and fewer defective flakes. In a typical process, 0.5 g $Ti_3AlC_2$ of MAX powder is mixed with 0.8 g LiF and 10 mL of 9 M HCl and stirred at room temperature for 24 h. Notably, after repeated washing, swelling of $Ti_3C_2$ is typically observed and the drying (typically 120 °C for 24 h in vacuum) is required for removal of water trapped between MXene layers. Hydrogen bifluoride

salts, such as $NH_4HF_2$ have also been reported to etch $Ti_3AlC_2$ MAX phase.[66] Typically, 0.5 g of $Ti_3AlC_2$ MAX powder could be completely etched with 10 mL of 2 M $NH_4HF_2$ solution at room temperature within 24 h. The presence of intercalated $NH_4^+$ can further increase the spacing between adjacent MXene layers.

Before 2018, only Al-containing MAX phases could be selectively etched. Recently, $Ti_3SiC_2$ MAX phase was successfully etched by oxidant-assisted selective etching method (Fig. 3a),[63] similar to the one used to etch SiC whiskers and produce SiC nanoplatelets.[64] In a typical process, 5 mL of 35 wt.% $H_2O_2$ is mixed with 45 mL of 30 wt.% HF to obtain an etchant solution. Then 3 g of $Ti_3SiC_2$ MAX powder is added into an etchant solution and stirred at 40 °C for 45 h. Besides $H_2O_2$, other oxidants were also used, such as $HNO_3$, $(NH_4)_2S_2O_8$, $KMnO_8$, and $FeCl_3$. The etching mechanism could be simply described as Si being oxidized by an oxidant and then reacted with HF (Fig. 3b-3d). This new method will largely expand the range of MAX phases precursors for MXenes.

When comparing synthesis of all of the reported MXenes, we can notice some general trends. First, synthesis of $M_{n+1}X_nT_x$ with larger *n* values typically needs stronger etchants and longer etching durations. Also, stronger etchants and longer etching durations are required for M elements with a higher atomic number. It can be reasonably inferred that this is related to the strength of M-A bonding, as higher atomic number indicates more valence electrons and stronger bonding.[25] Still, more experimental work is required, because for certain MXenes, etching with only 50 wt.% HF solutions have been reported and most MXene publications focus solely on $Ti_3C_2T_x$, while other MXenes have been studied much less.

In addition to solution based selective etching methods, high-temperature molten fluoride salts have also been used as etchants for MAX phases to leach out A elements as salts (for example $AlF_3$).[67] In the first report of the synthesis of nitride MXenes, instead of HF-based etchants, a mixture of various molten fluoride salts was used to selectively etch Al layers from the MAX phase $Ti_4AlN_3$, resulting in the $Ti_4N_3T_x$ MXene. $Ti_4AlN_3$ powder was mixed with a fluoride salt mixture, which contained 59 wt.% potassium fluoride (KF), 29 wt.% lithium fluoride (LiF), and 12 wt.% sodium fluoride (NaF). The mass ratio of $Ti_4AlN_3$ powder and fluoride salt was 1: 1. Then the mixture was heated to 550 °C for 30 min. After cooling down, the Al-containing salts were dissolved in $H_2SO_4$. It should be noted that HF-based etchants did not work for $Ti_4AlN_3$ MAX phase, with merely $Ti_4AlN_3$ nanosheets obtained after treating

$Ti_4AlN_3$ in an HF solution at room temperature. The reason for this will be discussed in Section 4.1.

Besides MAX phases, some non-MAX layered phases have also been used as precursors to produce MXenes, such as $Mo_2CT_x$, $Zr_3C_2T_x$ and $U_2CT_x$. $Mo_2CT_x$ was synthesized by selectively etching Ga layers from $Mo_2Ga_2C$.[68, 69] By contrast with the $Mo_2GaC$ MAX phase, which has only one layer of Ga separating carbide layers, there are two Ga layers between adjacent carbide layers, which facilitate etching. Furthermore, $Zr_3C_2T_x$ and $U_2CT_x$ were synthesized by etching out $Al_3C_3$ layers from $Zr_3Al_3C_5$ and $U_2Al_3C_4$ phases, respectively.[70, 71] The successful synthesis of these MXenes provides a new direction for the choice of precursor, which may expand the MXene family.

### 2.1.2. Delamination of multilayered MXenes

It is of particular interest to isolate single- or few-layer MXenes for both fundamental studies and fabrication of nanodevices. Unlike TMDs or graphene, the delamination of multilayered MXenes by mechanical exfoliation is challenging because of the strong interlayer interactions between adjacent MXene layers. To weaken the strong bonding, intercalation of organic molecules or ions is a feasible step, which has been widely used for other 2D materials. In 2013, the first study on the intercalation of $Ti_3C_2T_x$ MXene was reported by Mashtalir *et al.*[72] A broad range of organics and salts such as hydrazine, urea and dimethyl sulphoxide (DMSO) can be intercalated into $Ti_3C_2T_x$ MXene as confirmed by XRD patterns (Fig. 4a and b). For instance, the *c*-lattice parameter (*c*-LP) of $Ti_3C_2T_x$ increased from 19.5 Å to 25.5 Å after exposure to hydrazine, and it reversed to 20.1 Å when dried in vacuum at 200 °C. Among these intercalants, DMSO can expand the *c*-LP to 35.04 Å and even 44.8 Å after the sample is immersed for 3 weeks. This phenomenon can be attributed to the co-intercalation of water from environment and further exploited to fully delaminate MXenes to a colloidal solution of single- and few-layer flakes by sonication.[73] It should be noted that since the sonication time is usually long (up to 6 h), the lateral size of the flakes was decreased to hundreds of nanometers. Besides DMSO, isopropylamine was also able to delaminate $Nb_2CT_x$ by stirring for 18 h at room temperature (Fig. 4c and d).[48]

Other large organic base molecules can also be used as intercalants, including tetrabutylammonium hydroxide (TBAOH), tetramethylammonium hydroxide (TMAOH), choline hydroxide or *n*-butylamine.[74-76] TMAOH, one of the tetraalkylammonium compounds, has been

widely used for delamination of other 2D materials. The intercalation of $TMA^+$ ions into MXene layers by ion exchange with intercalated protons leads to swelling due to the expansion of interlayer spacing. Although manual shaking is enough for delamination of some 2D layered oxides, long stirring times (sometimes more than 12 h) or sonication is still needed in the case of MXenes intercalated with organic ions/molecules. As a result, the lateral size of MXene flakes in the stable colloidal solution is in the range between 200 to 700 nm, indicating that the intercalation of TMAOH can break the flakes down to smaller sizes.

Besides large organic molecules, various metal cations can also be intercalated into multilayered MXenes, such as $Li^+$, $Na^+$ and $K^+$.[77-79] In the HCl/LiF etching method, solvated $Li^+$ ions were intercalated into multilayered MXenes by ion exchange with protons. In the first report of this method (which is known as "clay" method), 30-60 min sonication was needed for delamination to get a stable colloidal solution.[46] As a result, the produced flakes were often small with many defects. Interestingly, when the LiF:$Ti_3AlC_2$ molar ratio was increased from 5 to ≥7.5 (mass ratio from 0.67 to ≥1) as well as the concentration of HCl increased from 6 to 9 M, *in situ* delamination of MXenes occurred even after hand shaking of the solution (this method is named "MILD" to describe the minimally destructive route to delaminate MXenes). Again, it should be noted that swelling was observed after selective etching, which is very important for delamination. The greatest advantage of MILD method is that the lateral sizes of flakes produced reach 3–6 μm with fewer defects due to elimination of sonication (Fig. 4e-h). This is preferable for fundamental studies and applications that require high-quality single MXene flake with high conductivity and mechanical strength.

The etching method also has a significant effect on the thermal stability. For example, Yu and co-workers reported that the complete transition temperature from $Ti_3C_2$ to anatase $TiO_2$ in air is higher for $NH_4HF_2$-etched $Ti_3C_2$ (500 °C) than HF-etched counterpart (350 °C).[80] In general, MXenes colloidal solution can be gradually oxidized with the presence of oxygen and light.[81] For the storage of MXenes, we suggest keeping colloidal solution in refrigerator which can decelerate the degradation rate. Oxygen-free degassed water is also recommended when storing MXene solutions.

As reviewed above, there are many different methods for producing MXenes. None of them is "perfect", but it is possible to select the most suitable routes for specific applications when considering lateral sizes, defects, colloidal solution concentration, etc.[82] Notably, post-treatments

can also be used to tune these parameters. Obviously, the flake sizes can be adjusted by sonication time and/or sonication power.[83] Previous work has also demonstrated that flakes with different sizes can be separated by centrifugation.[37] In addition, the defects density of flakes and solution concentration are largely dependent on synthesis routes.

## 2.2. Elemental analogues of graphene – silicene and germanene, produced by selective etching

After the big success of graphene, researchers looked into group IV elements in the periodic table. For example, silicon also has four electrons in its outermost *s* and *p* orbitals, as does carbon.[12] However, for silicon, the diamond structure with $sp^3$ hybridization is the energetically most favorable one and graphite-like allotrope of Si does not exist in nature. Hence, the synthesis of silicene by simple exfoliation of bulk Si precursors is implausible.

The research on silicene dates back to 1994, when Takeda and Shiraishi pointed out that silicon sheet may be an analogue of graphene, theoretically.[20] Silicene was grown on substrates such as Ir, Au and $ZrB_2$ by using epitaxial growth. Although the honeycomb structure of silicene had been confirmed and some properties studied, it was still necessary to remove the effect of substrates, obtaining a freestanding film or single crystal of silicene. In this context, researchers used topochemical deintercalation of $CaSi_2$ to produce hydrogen-terminated silicene (silicane, by analogy with graphane) or layered polysilane (Fig. 5a and b).[18] $CaSi_2$ belongs to the family of Zintl silicides and is perfectly suitable for selective etching because it has alternately stacked layers of interconnected 2D corrugated bilayers (silicene, honeycomb structure) and Ca monolayers.

The research on removing $Ca^{2+}$ from Zintl phase of $CaSi_2$ has a long history. The basic idea of this topochemical deintercalation is to selectively etch $Ca^{2+}$ from $CaSi_2$ without destroying the silicon backbone, which is further terminated (e.g., neutralized by the protons of HCl) or oxidized to form layered silicane or polysilane.[12] The silicon backbone can be preserved due to the strong Si=Si bonding in the silicon layers, while $Ca^{2+}$ is leached out as $CaCl_2$. In 1961, Bonitz and co-workers reported the selective etching of $Ca^{2+}$ from $CaSi_2$ by using $Cl_2$,[84] similar to carbide derived carbon synthesis.[85] The drawback of this method is that the resultant silicon sheets were too reactive and unstable, which hindered the use of this synthesis method. Another approach is to use HCl instead of $Cl_2$. As we mentioned before, HCl can selectively react with Ca forming $Ca^{2+}$ ions and the residual silicon backbone will be neutralized by $H^+$. Interestingly,

the termination of silicane can be easily tuned by simply using different HCl solutions. When treating $CaCl_2$ in low-temperature (below -30 °C) HCl aqueous solution, hydrogen-terminated silicon sheets (silicane, $Si_6H_6$) can be obtained (equation 1), while $Si_6H_3(OH)_3$ was formed when the treatment temperature was 0 °C (equation 2). In addition, if the topochemical deintercalation was conducted in HCl solution in methanol or ethanol, the product was $Si_6H_3(OCH_3)_3$ or $Si_6H_3(OC_2H_5)_3$ (equation 3).[12, 14, 15, 19]

$$3CaSi_2 + 6\ HCl \rightarrow (SiH)_6 + 3\ CaCl_2 \quad (1)$$

$$3CaSi_2 + 6HCl + 3H_2O \rightarrow Si_6H_3(OH)_3 + 3CaCl_2 + 3H_2 \quad (2)$$

$$3CaSi_2 + 6HCl + 3TOH \rightarrow Si_6H_3(TO)_3 + 3CaCl_2 + 3H_2 \quad T= \text{methyle, ethylene} \quad (3)$$

The delamination of multilayer silicane sheets to single- or few-layer sheets was attempted by dispersing siloxene $Si_6H_3(OH)_3$ solids in sodium dodecylsulfate (SDS) and shaking at room temperature for 10 days (Fig. 5c~ e). During delamination, $H_2$ was generated which suggested the oxidation of $Si_6H_3(OH)_3$. The delaminated nanosheets had lengths around 100-200 nm with thicknesses of 0.7 nm. To obtain high quality monolayer silicane sheets, researchers tried to reduce the charge on silicon layers. This is because $CaSi_2$ is ionic so there is a strong electrostatic bonding between $Ca^{2+}$ and $Si^-$. Nakano et al. reported the synthesis and topochemical deintercalation of Mg-doped $CaSi_2$ ($CaSi_{1.85}Mg_{0.15}$).[16] A stoichiometric mixture (Ca:Si:Mg=1:1.85:0.15) of CaSi (99%), Si (99.99%), and Mg (99.9%) was used as the starting materials and melted in a water-cooled copper crucible with radio-frequency (RF) heating under an Ar atmosphere and then slowly cooled to room temperature. The propylamine hydrochloride (PA·HCl) aqueous solution was reacted with $CaSi_{1.85}Mg_{0.15}$ and the mixture was stirred at room temperature for 10 days. Subsequently, a light-brown silicon sheet suspension was obtained with a total yield less than 1%. The produced sheets had lateral sizes between 200 and 500 nm and an average thickness of 0.37 nm. Tchalala *et al.* synthesized $K_{2x}Ca_{1-x}Si_{2-x}$ by mixing potassium (K) with $CaSi_2$ at 160 °C. After reaction with PA·HCl, a greenish-brown suspension was formed with a much higher yield of 20% (Fig. 5f ~k).[86]

The electron configuration of germanium is similar to silicon due to 4 valence electrons. Accordingly, it was possible to synthesize single-atom thick germanium layers after silicon nanosheets. Similarly, topochemical deintercalation of layered Zintl phase $CaGe_2$ to obtain layered germanium solids has been studied extensively. In 2013, Goldberger *et al.* first reported the synthesis of multilayer hydrogen-terminated germanium (germanane, GeH) with millimeter-

scale flakes (around 2-6 mm) from the topochemical deintercalation of $\beta$-$CaGe_2$ (Fig. 6a).[11] To synthesize $\beta$-$CaGe_2$, Ca and Ge were first put in a quartz tube with stoichiometric ratios and evacuated to milliTorr pressures before sealing. Then, the tube was annealed at 950-1050 °C for 16-20 h and cooled down to room-temperature over 1-5 days. The resultant $CaGe_2$ had unit cell parameters of a = 3.987 Å, c = 30.0582 Å, as confirmed by XRD pattern. To de-intercalate Ca, $\beta$-$CaGe_2$ was placed in concentrated HCl with stirring at -40 to -20 °C for 5 to 10 days. Finally, the collected GeH was washed by deionized (DI) water and methanol to remove residual $CaCl_2$ and dried at room temperature. The multilayer GeH had a diameter around 2-3 mm and thickness less than 100 μm.

XRD analysis showed that 2H GeH was synthesized in this way with an expansion in *c*-direction (out of plane) and a slight contraction in *a*-direction (in-plane) (Fig. 6b). From energy dispersive X-ray spectrum (EDS), it was obvious that the signal of Ge was very high with the absence of Ca and O. Although there were trace amounts of Cl, the Cl:Ge ratio was as low as 0.02. The hydrogen termination was further confirmed by a systematical study with Fourier-transform infrared spectroscopy (FTIR), Raman spectroscopy and X-ray photoelectron spectroscopy (XPS). Ge-H stretching (~ 2000 $cm^{-1}$), Ge-$H_2$ bending (770 and 825 $cm^{-1}$) and Ge-H wagging (475 $cm^{-1}$) modes were confirmed in FTIR by comparing with GeD (treating $CaGe_2$ in 95% deuterated $DCl/D_2O$) as shown in Fig. 6f. In contrast to crystalline germanium, there are two features for GeH in Raman spectra (Fig. 6g). First, the Ge-Ge stretch is blue-shifted to 302 $cm^{-1}$ and second, another vibration mode appeares at 228 $cm^{-1}$, which was predicted as $A_1$ mode by theoretical calculations. Importantly, it was found that GeH is very stable in ambient atmosphere because there was no presence of Ge-O in FTIR, even after two months. This feature is of crucial importance for many optical and electronic applications.

In addition, the thermal stability was studied, showing that GeH is thermally stable up to 75 °C, above which amorphization begins to occur, being complete at 175 °C. The dehydrogenation process occurs from 200 to 250 °C. Monolayer GeH was also achieved by exfoliating multilayer GeH. Theoretically, the interlayer bonding mode of GeH was proven to be van der Waals interaction with a binding energy of 72 meV/Ge atoms, which is similar to the case of graphite. Accordingly, both Scotch tape and polydimethylsiloxane were used to exfoliate multilayer GeH, resulting in single- to few-layer GeH flakes (Fig. 6e).

In 2014, methyl-terminated germanane ($GeCH_3$) was synthesized by a one-step metathesis approach during exfoliation of $CaGe_2$ crystals.[13] $CaGe_2$ crystals were reacted with biphasic $CH_3I/H_2O$ solvent, followed with rinsing in HCl and isopropanol. The single-crystalline hexagonal structure of $GeCH_3$ was confirmed by XRD with apparent expansion along the *c*-direction (3.1 Å per layer). This increase further demonstrated the substitution of H-termination with $CH_3$-termination. $GeCH_3$ is thermally stable to 250 °C.

## 3. SYNTHESIS OF 2D MATERIALS BY TOPOCHEMICAL TRANSFORMATION FROM NON-LAYERED PRECURSORS

Thus far, layered materials, such as graphene, $MoS_2$ and MXenes, have been exfoliated and widely explored and demonstrated promise in (opto)electronics, energy conversion, harvesting and storage.[87-90] Non-layered material have crystal structures in which chemical bonds exist in long range in all three dimensions. Due to the difficulty of bond-cleavage of non-layered compounds and the lack of an intrinsic driving force for two-dimensional anisotropic growth, it is a challenge to synthesize 2D materials from non-layered precursors. Recently, a series of 2D non-layered materials including metals, metal oxides, nitrides, carbides, chalcogenides, organic-inorganic hybrid perovskites, etc., have been prepared by wet chemistry methods and van der Waals epitaxial (vdWE) growth, which have been summarized in a previous review.[91]

### 3.1. Template-assisted synthesis of 2D non-layered materials

Recently, template-assisted methods have been demonstrated as promising strategies to synthesize 2D materials that have no layered precursors. Metal precursors on the template's surface can be topochemically transformed into metal oxides, nitrides, carbides or other 2D materials.

2D transition metal oxides (TMOs) with exotic electronic properties and high specific surface areas have demonstrated promise in applications ranging from electronics to energy storage. Unlike layered metal oxides, including $\alpha$-$MoO_3$ and birnessite $MnO_2$, which can be exfoliated into 2D nanosheets, traditional methods are not feasible for the synthesis of majority of 2D TMOs.[92,93]. Salt-templating strategy recently showed promise for synthesis of many oxides as depicted in Fig. 7a.[22] Typically, a metal precursor solution is first dissolved in ethanol and then mixed with NaCl or KCl salt (labeled precursor@salt). After drying, the salt precursor is annealed at an elevated temperature to produce 2D oxides@salt, the 2D oxides having grown on

the surface of the salt. The salts are removed by dissolving the product in DI water and then the 2D nanosheets are collected by vacuum filtration.

Here, the salt microcrystals served as the substrate/template to guide the oxide growth at elevated temperatures. By virtue of the lattice match of the crystal face of salt and target oxide, the synthetic mechanism was proposed to be Frank–van der Merwe mode film growth and possible heteroepitaxy.[94] Using the synthesis of 2D *h*-$MoO_3$ as an example, a precisely calculated amount of precursor was loaded to restrict the growth of thick nanosheets, and NaCl microcrystals were used as lattice-matched templates. Fig. 7b shows the growth of *h*-$MoO_3$ on the surface of NaCl. The formation of *h*-$MoO_3$ rather than $\alpha$-$MoO_3$ is not only due to the lattice match-induced *h*-$MoO_3$ nucleation but also attributed to $Na^+$ ions serving as a mineralizer and stabilizer of the hexagonal tunnels of *h*-$MoO_3$.[95] The XRD pattern (Fig. 7c) reveals the similar close pairing of the diffraction peaks between the (140) peak of *h*-$MoO_3$ and the (220) peak of NaCl templates. As shown in Fig. 7d, the scanning electron microscopy (SEM) image of as-prepared 2D *h*-$MoO_3$ confirms a larger size than that of liquid-exfoliated or chemically synthesized nanosheets.[96] The transmission electron microscopy (TEM) image (Fig. 7e) further confirms the planar 2D morphology with high transparent and wrinkled sheets, with an average flake thickness of 1.55 nm, as determined by atomic force microscopy (AFM, Fig. 7f). More importantly, such a facile synthetic strategy can be extended to prepare various 2D oxides with non-layered structure, including $MoO_2$, MnO and *h*-$WO_3$.

Most recently, Zavabeti *et al.* reported a liquid metal-based reaction route, which used room-temperature liquid metals as a reaction environment to synthesize 2D oxides ($HfO_2$, $Al_2O_3$, and $Gd_2O_3$) that were previously inaccessible with pre-existing methods.[97] Two novel synthetic strategies and also the representative TEM images of 2D $HfO_2$ are shown in Fig. 8a-d. The surface of a liquid metal droplet could be topochemically transformed into ultrathin 2D oxide nanosheets by exposure to air. As shown in Fig. 8a, the oxide skin on the liquid parent metal is cast on the substrate by the liquid metal droplet when it touches the substrate. There are no strong forces acting between the metal and its oxide skin, which allows clean delamination.[98] As shown in Fig. 8b, the TEM images of as-synthesized high-quality 2D $HfO_2$ confirms its 2D nature with translucent appearance and occasional wrinkles, while high-resolution TEM (HRTEM) and electron diffraction demonstrate polycrystallinity. The second technique relies on the injection of pressurized air into the liquid metal (Fig. 8d). The metal oxide rapidly forms on

surface of air bubbles as they rise through the liquid metal (GaInSn alloy with other metals dissolved). Then, the bubbles pass through DI water above the liquid metal, allowing the produced oxide sheets to be dispersed into an aqueous suspension. Such a technique is scalable and suitable for creating high yield suspensions of the target oxide nanosheets. The obtained 2D $HfO_2$ is similar to the exfoliated $HfO_2$ (Fig. 8c). Using the liquid-metal strategy, more 2D materials have been prepared, including GaS,[99] $GaPO_4$,[100] SnO,[101] etc.

Besides the salt-templated and liquid metal strategy, many other novel templating strategies have also been developed. By using graphene as a sacrificial template, 2D metal oxides, including $SnO_2$, $Fe_2O_3$, $NiFe_2O_4$, $TiO_2$, $Nb_2O_5$, and $Mn_2O_3$, can be synthesized.[102-106] Metal ions are first adsorbed on the surface of graphene or graphene oxide (GO). Then, after annealing in air, the graphene or GO are removed and metal oxide nanosheets are topochemically formed from metal ions. Cheng *et al.* synthesized 2D $\alpha$-$Fe_2O_3$ nanosheets based on a "template-assisted oriented growth" strategy, in which CuO sheet served as template.[107] Also, Zhou's group reported a molten salt method for the high-yield synthesis of 2D metal oxides, including $Na_2W_4O_{13}$ and $K_{0.27}MnO_2{\cdot}0.54H_2O$.[108] The molten salt derived ionized species rapidly reacted with the precursor to form the 2D materials, which could be easily recovered by dissolving the salts. All of these 2D metal oxides have similar atomic structures in which ions intercalate into the interlayers.[109]

While a number of 2D transition-metal carbides (MXenes) have been reported, 2D metal nitrides are limited to merely a handful of reported materials, such as $Ti_4N_3$ MXene,[25] MoN,[110] and GaN.[111] Transition-metal nitrides usually show a higher conductivity than their respective carbides in bulk state. Currently, 2D nitrides are mainly produced by exfoliation of layered materials (*h*-BN) and gas-phase syntheses (2D GaN).[112,113] Since most metal nitrides form non-layered structures, exfoliation methods are not promising. Inspired by the salt-templating strategy mentioned above, 2D non-layered metal nitrides have also been synthesized by using non-layered 2D metal oxides as precursors, which were directly ammoniated to obtain nitrides.[114] Typically, as shown in Fig. 9a, the Mo precursor@NaCl powders were firstly annealed in Ar to form 2D *h*-$MoO_3$@NaCl, which was then slowly ammoniated in ammonia, $NH_3$, to form 2D MoN@NaCl. During the synthesis process, the salt can serve as a stabilizer to prevent collapse of the sheets and maintain 2D morphology. Side (Fig. 9b) and top (Fig. 9c) views of a MoN monolayer show 6 layers of atoms and thickness of around 0.7 nm. As shown in Fig. 9d, the high

density of states (DOS) at the Fermi level reveals metallic properties of MoN. The large partial DOS at the Fermi level is mainly achieved by the *d* electrons of Mo atoms, resulting in the high conductivity of 2D MoN. Overlapping transparent flakes of MoN displayed in the TEM image (Fig. 9e) confirm subnanometer thickness. HRTEM and corresponding selective area electron diffraction (SAED) patterns shown in Fig. 9f verify the hexagonal structure of MoN. Following the same strategy, 2D $W_2N$ and $V_2N$ were also prepared.[114] Meanwhile, Xiong *et al.* used this salt-templated synthesis method to prepare 2D defect-rich MoN nanosheets by an incomplete ammoniation of $MoO_3$ nanosheets.[115] In addition, this salt-templating strategy was successfully extended to synthesize 2D carbides.[116] The $MoO_3$@NaCl crystals were annealed in an atmosphere of $H_2/CH_4$, during which $MoO_3$ was synchronously reduced to Mo and carbonized to $Mo_2C$ to obtain $Mo/Mo_2C$ nanosheets. In general, for these 2D transition metal nitrides or carbides, O-terminations or trace amounts of oxides are always present in the materials as long as they are exposed to air.

### 3.2. Transformation from 2D metal oxides or hydroxides to 2D materials

Besides the template-assisted method, other topochemical transformations are also considered as a facile strategy to synthesize 2D non-layered materials.[117-121] For instance, Wu's group has synthesized 2D *d*-FeOOH nanosheets from $Fe(OH)_2$ nanosheets.[122] Atomic structure analyses (Fig. 10a) reveal that $Fe(OH)_2$ and *d*-FeOOH have similar crystal planes, which have very similar (001) facets (4.605 Å for $Fe(OH)_2$ and 4.530 Å for *d*-FeOOH). It suggests that ultrathin *d*-FeOOH nanosheets can be obtained by a facile topochemical transformation strategy. Experimentally, 2D *d*-FeOOH ultrathin nanosheets with less than three unit cells were obtained *via* the oxidation of $Fe(OH)_2$ ultrathin nanosheets. The TEM image (Fig. 10b) shows large-area transparent wrinkled 2D *d*-FeOOH, confirming the ultrathin nanosheet. Zhu *et al.* reported a facile and scalable synthesis of high-quality ultrathin 2D nanosheets of lamellar nickel hydroxides and topochemical non-layered nickel oxides.[123] As shown in Fig. 10c, first, ultrathin lamellar nickel hydroxide ($\alpha$-$Ni(OH)_2$) was prepared by a liquid-phase microwave irradiation method, using homogeneous alkalization of nickel(II) nitrate solutions by urea hydrolysis through inductive effect of microwave irradiation under moderate temperature and atmospheric pressure.[124] The rapid microwave heating can lead to super-saturation of reactant species, instantaneous formation of ultrafine nanocrystals, and then spontaneous self-assembly by intrinsic driving force of lamellar nickel hydroxide for 2D anisotropic growth. After heat

treatment at 300 $^{o}$C, $\alpha$-$Ni(OH)_2$ nanosheets are completely decomposed into NiO. The as-synthesized $\alpha$-$Ni(OH)_2$ precursor exhibits a sheet-like structure (Fig. 10d). The sheets are uniform and freestanding with a micron-sized planar area. The nanosheets are comprised of ultrafine nanocrystals arranged in plane. The sheet-like morphology can be perfectly retained after heat treatment (Fig. 10e), and there are no apparent broken or collapsed structures in the final product, suggesting good structural stability of this 2D structure. Enlarged SEM images (Fig. 10f) further reveal a highly flexible and gauze-like morphology of non-layered NiO.[125]

Wu *et al.* have developed a combinatorial self-regulating acid etching and topochemical transformation strategy to prepare vertically stacked ultrathin 2D non-layered nickel selenide (NiSe) nanosheets.[126] Due to inhibited hydrolysis under acidic conditions, the self-regulating acid etching results in ultrathin layered $Ni(OH)_2$ (two layers). The ultrathin structure allows limited epitaxial extension during selenization, enabling facile artificial engineering of hydroxide foundation frameworks into ultrathin non-layered selenides. As illustrated in Fig. 10g, a self-limiting tunable acid etching was firstly proposed[126] to prepare hierarchical ultrathin 2D layered $Ni(OH)_2$ nanosheets, followed by transforming into ultrathin non-layered NiSe nanosheets. With the pH self-regulation, *in situ* etching of Ni foam that simultaneously serves as a Ni source and support brings in superior interfacial contact, leading to a two-tiered interlaced ultrathin nanosheet structures. Significantly, unlike the bulky structures that succumb to excessive lattice expansion, the elaborate ultrathin layered frameworks allow nondestructive selenization to topochemically transform into non-layered counterparts. As shown in Fig. 10h, the ultrathin nanosheet structure is well retained after the selenization treatment.

Following the precursor morphology-directed strategy,[127] Xu *et al.* prepared 2D nickel nitride nanosheets by direct calcination of the Ni-based precursor nanosheets at 380 °C under an $NH_3$ atmosphere.[128] The overall reaction can be described using the equation 4:

$$6Ni(OH)_2 + 4NH_3 \rightarrow 2Ni_3N + 12H_2O + N_2 \quad (4)$$

Calculated DOS of bulk $Ni_3N$ is continuous near the Fermi level, indicating that $Ni_3N$ is intrinsically metallic (Fig. 11a). Near the Fermi level, the DOS intensity of $Ni_3N$ sheet is higher than that of bulk $Ni_3N$, indicating that dimensional confinement can improve the electrical properties of $Ni_3N$. SEM images (Fig. 11b) demonstrate that the as-prepared $Ni_3N$ samples consist of uniform 2D nanosheets with unique porosity, which is also confirmed by the TEM image (inset of Fig. 11c). The HRTEM image and corresponding fast Fourier transform (FFT)

pattern (Fig. 11c) clearly reveal that the nanosheet is a hexagonal single crystal with *c*-axis crystalline orientation. With a similar method, Xie *et al.* successfully grew $Ni_3N$ nanosheets on a Ti plate, which was further used as a non-enzymatic electrochemical glucose sensor superior in analytical performance.[129] 2D materials can also be prepared by topochemical transformation from 2D non-layered metal oxides. Zhou's group synthesized 2D $Mo_2C$ and N-doped $Mo_2C$ (N-$Mo_2C$) nanosheets through a topochemical transformation method.[130] Typically, the N-$Mo_2C$ nanosheets were synthesized by reacting with dissociative C and N produced by decomposition of dicyandiamide with $MoO_2$ nanosheets at 700 °C. 2D $Mo_2C$ nanosheets could be obtained under the same conditions with glucose replacing dicyandiamide. As shown in Fig. 11d, the (200) and (002) planes were perpendicular to the $MoO_2$ and N-$Mo_2C$ nanosheets, with interplanar spacings of 0.241 nm and 0.237 nm, respectively. The $MoO_2$ nanosheets exhibited a hexagonal morphology of several micrometers and possessed a smooth surface and edges (Fig. 11e). Clearly, the resulting N-$Mo_2C$ (Fig. 11f) retains the nanosheet structure with coarse surfaces, which exhibit excellent activity for hydrogen evolution reaction.

## 4. TRANSFORMATION OF 2D METAL DISULFIDES, CARBIDES AND NITRIDES

Besides 2D metal oxides and hydroxides, other 2D materials can also be used as precursors for synthesis of another 2D material *via* transformation. These transformations include carbide MXenes to nitride MXenes and transforming transition metal sulfides to transition metal carbides and nitrides.

### 4.1. Topochemical transformation of carbide MXenes to nitride MXenes

Theoretically, the same number of carbide MXenes should exist as nitride MXenes. It was not until several years after discovery of the first carbide MXene, $Ti_3C_2$, when the first nitride MXene $Ti_4N_3$ was made.[67] This was followed by the report of the synthesis of $Ti_2N$ by the selective etching of $Ti_2AlN$ MAX phase.[131] For the most part, however, exfoliation of MAX phases in aqueous hydrofluoric acid solutions, a common approach for synthesizing carbide MXenes, has not been successful for the majority of nitride MAX phases. Nitride MXenes are unstable in aqueous hydrofluoric acid, unlike carbide MXenes. This may be related to how the formation energies of nitride MXenes (e.g., $Ti_{n+1}N_n$) from their MAX phase precursors (e.g. $Ti_{n+1}AlN_n$) are greater than those of carbide MXenes from their corresponding MAX

precursors.[132] Moreover, cohesive energies of nitride MXenes are lower than those of corresponding carbides.[132] Therefore, chemical etching of nitride MAX phases in aqueous hydrofluoric acid to yield 2D metal nitrides has been unsuccessful because it is difficult to selectively etch the MAX phase without dissolving the unstable product.

An alternate route, high-yield gas-phase synthesis seem to be promising for synthesizing 2D metal nitrides. Although synthesis of 2D metal nitrides through CVD methods has not been demonstrated, the synthesis of two novel transition metal nitrides *via* ammoniation and nitridation of carbide MXenes at elevated temperatures, has recently been reported.[133] During the treatment, carbon from carbide MXenes can be topochemically substituted by N, resulting in a nitride MXene with a similar structure. This demonstrates that topochemical transformation of precursors into 2D metal nitrides is not limited to metal oxides. Nitridation of 2D metal carbides offers a route to synthesis of 2D metal nitrides which do not have bulk precursors that can be selectively etched.

The complete nitridation of 2D metal carbide MXenes, $Mo_2C$ and $V_2C$, was recently reported.[133] Although incomplete nitridation of certain MXenes, including $Ti_3C_2$, has been reported,[134] this technique has potential to produce 2D metal nitrides from the widely available MXene carbide precursors. Typically, films of delaminated $Mo_2CT_x$ and $V_2CT_x$ flakes were heated separately at 600 °C for 1 h in anhydrous ammonia. For $Mo_2C$ and $V_2C$, after ammoniation, characterization determined that $Mo_2N$ adopted a buckled MXene structure while $V_2C$ transformed into a mixed layered structure of trigonal $V_2N$ and cubic VN. Various temperatures were examined to see the change in the ratio of nitrogen to carbon content after treatment. As temperature increased from 400 to 600 °C, the amount of N relative to C greatly increased for both carbide reactants, suggesting that nitridation occurred. XPS analysis was performed to confirm that N was bonded to the metal atoms of either product (Mo or V), and that C-metal bonding was eliminated or greatly decreased.

XRD was also performed to determine the crystal structure. In Fig. 12a, after ammoniation of $Mo_2CT_x$, the pattern of the product $Mo_2N$ (red, second curve from bottom) showed a (002) peak at $2\theta = 11°$, which is typical for $M_2X$ MXenes. This basal plane peak represents the distance between MXene layers, and its value depends on the type of MXene and intercalated molecules and water.[135, 136] For the synthesized $Mo_2N$, the value of the position indicates that there are no intercalated molecules between the layers. The presence of (004) and (006) peaks indicates

higher ordering of the layers. For the vanadium nitride sample (top curve), the (002) peak shifted from 8-9° to 7.0° after ammoniation, suggesting that the spacing between layers has increased. A new peak appearing at 37°, however, can be attributed to the (111) peak of cubic VN, suggesting that a new non-MXene phase has formed.[137, 138]

X-ray pair distribution function (PDF) analysis was then performed to obtain a more precise quantification of the atomic structure and morphology. The measured PDF vanadium product (blue curve) indicates that in the high-*r* region (up to $r$ = 60 Å) was well fit to a trigonal $V_2N$ structure (space group $P\bar{3}1m$). It was further determined that having a second, less prominent phase, cubic VN (space group $Fm\bar{3}$m) was present with the trigonal $V_2N$ providing a better fit, shown by the red curve in Fig. 12b. The green curve shows the offset between the measured and theoretical curves of this mixed phase. For the $Mo_2N$ product (shown schematically in Fig. 12c), it was determined that the measured PDF (top blue curve in Fig. 12d) matched best with a buckled single slab MXene structure (top red curve). The measured PDF did not match well with the typically non-buckled MXene structure (middle brown curve).

In terms of electrical conductivity, bulk metal nitrides are superior to their carbide counterparts.[139] In this work, temperature-dependent resistivity measurements were performed on the nitrides. Interestingly, $Mo_2N$ had room-temperature electrical conductivity values three orders of magnitude larger than its $Mo_2CT_x$ precursor. The $V_2N$+VN mixed phase has room-temperature electrical conductivity values one order of magnitude higher than its $V_2CT_x$ precursor. Moreover, the conduction mechanisms for both products change, both adopting metallic behavior after nitridation. The high conductivity of these nitride MXenes indicates potential applications in energy storage, electrocatalysis and beyond.

### 4.2. Transition metal nitrides or carbides produced from transition metal sulfides

The topochemical transformation of 2D materials into 2D metal nitrides has also been studied on other candidates such as TMDs. Actually, TMDs, including transition metal disulfides like $MoS_2$ have been used to synthesize not only transition metal nitrides, but also carbides. For some nitrogen-rich metal nitrides, such as $MoN_2$ which has been proven to be a very good catalyst, the synthesis conditions of the bulk precursor are very harsh (very high temperature and high pressure), not to mention the exfoliation process to obtain 2D single layers. It is therefore important to investigate other topochemical synthesis techniques, for example *in situ* substitution of S in $MoS_2$ with N or C can ideally achieve $MoN_2$ or $MoC_2$. Recently, some related studies

have been reported,[140,141] and there is no doubt that these topochemical synthesis methods could largely expand the family of 2D materials.

### 4.2.1. Conversion of molybdenum disulfide to molybdenum carbide

2D molybdenum carbide has potential to be promising hydrogen evolution reaction (HER) catalysts,[133] and act as anode materials in Li-ion batteries.[131] In general, molybdenum carbides have been synthesized by several methods, which includes the carburization of $MoS_2$,[142, 143] *via* etching of Ga from $Mo_2Ga_2C$,[68, 135] and use of $MoCl_5$ as a precursor.[144] Although $\alpha$-$Mo_2C$ nanosheets have been synthesized *via* CVD methods, this requires high-temperature processes in a specific temperature range and the thickness was not less than 2.5-3 nm.[5] Epitaxial synthesis of $Mo_2C$ on $MoS_2$ *via* the carburization of exfoliated $MoS_2$ was investigated as an alternative to etching techniques and CVD techniques that require higher temperatures.[23]

Using Cu foil as a catalyst, $MoS_2$ flakes were annealed at 820 °C in a $CH_4$ and $H_2$ environment.[23] Fig. 13a shows a schematic of the mechanism of $Mo_2C$ growth on $MoS_2$. As supported by DFT results, this process begins at the edges of $MoS_2$. Hydrodesulfurization occurs by the detachment of S atoms at the edge, due to a reaction of the S atoms with H• radicals and $CH_3$• radicals combined with the Mo-terminated edge (dotted red box in Fig. 13a). The radicals are formed by decomposition of the $CH_4$ molecules in the presence of Cu. An $H_2S$ byproduct is formed by the reduction of S atoms near the $CH_3$-terminated Mo. The Mo and C form C–Mo–C bonds which then extend laterally.

The area of conversion increased with annealing time, and complete conversion of $MoS_2$ to $Mo_2C$ occurs after 4 h. Conversion to $Mo_2C$ is indicated by XPS analysis showing a shift of the doublet Mo $3d_{5/2}$ and $3d_{3/2}$ to lower binding energies, corresponding to Mo atoms being in the $Mo^{2+}$. Fig. 13b shows that after 4 h of annealing in $CH_4$ and $H_2$, there is complete conversion of $MoS_2$ to $Mo_2C$ indicated by the change increased intensity of the $Mo^{2+}$ component and disappearance of the $Mo^{4+}$ component.

Fig. 13c and d show optical microscope images of a few-layered exfoliated $MoS_2$ flake before and after 3 h of annealing, respectively. In Fig. 13d, the red dotted area demonstrates fully converted $Mo_2C$, while the green dotted area shows unconverted $MoS_2$. Raman spectra shown in Fig. 13e show which areas are composed of $MoS_2$ or $Mo_2C$. Point 1 ($MoS_2$ before annealing) and point 3 (unconverted $MoS_2$ after annealing) show the $A^1_g$ out-of-plane vibration mode of sulfur atoms at 406 $cm^{-1}$ and $E^1_{2g}$ in-plane vibrations of molybdenum and sulfur atoms at 382 $cm^{-1}$. In

point 2, corresponding to the half-down side of the flake with the $Mo_2C$ formed after 3 h of annealing, two peaks appear at 140 and 240 $cm^{-1}$ which may correspond to $2E_g$ (in-plane) and $A_{1g}$ (out-of-plane) vibration modes of $Mo_2C$.[145] Furthermore, the vibration modes corresponding to $MoS_2$, present in points 1 and 3, are not present in point 2.

The Raman mapping shown in Fig. 13f, g and h show the $A_{1g}$ modes of $MoS_2$ (blue) and $Mo_2C$ (red) at different annealing times. Fig. 13g exhibits conversion from $MoS_2$ to $Mo_2C$ that is initiated at the edges, while Fig. 13h shows that with longer annealing, conversion increases, as the bottom side of flake is converted to $Mo_2C$, as well as the partial edge of the $MoS_2$ of the upper side. Fig. 13i, j and k show work function mapping of the same images, attained by Kelvin probe force microscopy (KPFM), to reveal the work function across the area of the $MoS_2$ and $Mo_2C$ samples. The work function of the $MoS_2$ was found to be 4.3 eV, as predicted from theoretical calculations.[145] The color difference between the synthesized $Mo_2C$ (bright region) and unconverted $MoS_2$ (dark region), show the difference in work function between the two materials. The $Mo_2C$ synthesized was found to have a higher work function of 4.45 eV. These results were corroborated by TEM images. This $Mo_2C$ also showed promising sheet resistance of 123.6 $\Omega$ $sq^{-1}$ and carrier concentration of $5.84 \times 10^{13}$ $cm^{-2}$. This work showed the successful transformation of a 2D transition metal sulfide to a 2D transition metal carbide $Mo_2C$.

### 4.2.2. Conversion of 2D metal sulfides and selenides to molybdenum nitride

While the transformation of 2D oxides and carbides into 2D nitrides has been reported, [114,132] other 2D metal compound precursors are also available and should be considered. There have been reports on the transformation of transition metal chalcogenides to 2D metal nitrides.[146,147] Transition metal chalcogenides GaS and GaSe have been transformed to GaN *via* nitridation.[146] In nitridation *via* ammoniation, precursors are typically treated in ammonia at high temperature. In the first report of the synthesis of GaN, precursor GaS or GaSe nanosheets were treated in ammonia at 600-650 °C.[147] These materials were chosen as precursors because both adopt morphology similar to mica and can undergo micromechanical cleavage. Either precursor undergoing ammoniation at 650 °C (for GaS) or 600 °C (for GaSe) yields GaN with wurtzite crystal structure. EDS and XRD analyses confirm that GaS and GaSe are absent after nitridation. This treatment yields nanosheets with thicknesses of 1.8 nm (for GaN synthesized from GaS) and 3.0 nm (GaN from GaSe precursor). To yield single-layer GaN, single-layer GaS or GaSe must be deposited on a solid substrate, which then undergoes nitridation.

Transition metal dichalcogenides are also candidates for nitridation. Molybdenum disulfide has not only been used as a precursor to synthesize carbides. The synthesis of 2D molybdenum nitrides *via* nitridation of 2H-$MoS_2$ has been recently reported.[148] This yielded 2D $Mo_5N_6$, MoN or $Mo_2N$, depending on the temperature of nitridation. Reaction temperatures for nitridation were determined by measuring weight change during the reaction of $MoS_2$ powders in ammonia at elevated temperatures.[148] Thermogravimetry and differential thermal analysis (TG-DTA) was applied in non-isothermal treatments up to 1250 °C in an argon atmosphere. In order to investigate the reaction with ammonia, the environment was changed from argon to ammonia at specific temperatures. It was determined that the final mass loss of 29.95%, achieved at 750 °C, corresponds well to the theoretical mass loss of $Mo_5N_6$ (29.5%). This suggests that at 750 °C, $NH_3$ reduces $MoS_2$ first to $Mo_5N_6$ (Fig. 14a). By reducing $MoS_2$ at 920 °C, TG, differential thermal gravimetry (DTG), and DTA curves show that mass loss increases to 30.6%, which corresponds to the formation of MoN (Fig. 14b). With higher weight loss $Mo_2N$ (Fig. 14c, d) is also formed. When ammoniation is performed at 1020 °C, MoN and then $Mo_2N$ are formed depending on the duration and mass loss. $Mo_2N$ may decompose to Mo after a certain time of reaction, indicated by high mass loss. At the last investigated temperature of 1120 °C, DTG and DTA curves suggest that two reactions occur: the generation of $Mo_2N$ and its decomposition to Mo (Fig. 14e) and other byproducts. XRD analysis also confirmed the formation of phases at various temperatures and mass losses.

This extensive study showed the formation of several 2D molybdenum nitrides across temperature regimes and duration of treatment in ammonia. While this is only the first report on nitridation of a TMD, there is potential for synthesis of other 2D metal nitrides *via* nitridation of various TMDs.

## 5. CONCLUSIONS AND PERSPECTIVES

In this review, we discussed the recent developments of topochemical synthesis of 2D materials. Two approaches, topochemical deintercalation and phase transformation are most frequently used. A typical deintercalation method involves selective etching and can generate many new 2D materials by selectively removing certain element layers or compounds from a parent precursor. The feasible precursors are those bonded by weak van-der-Waals forces along one direction. For example, MXenes can be obtained by selectively etching A element from MAX phase; germanane was synthesized through selective removing $Ca^{2+}$ from $CaSi_2$; $Al_3C_3$ layers are etched

out from $Zr_3Al_3C_5$ to form $Zr_3C_2T_x$. In general, the choice of etchant and etching process are of particular importance for this method. When using MILD method containing optimal ratio of LiF/HCl to MAX, larger and higher quality MXene flakes are attained. The termination of germanane could be modified by controlling the etching process. On the other hand, for some 2D materials there is no feasible precursors for selective etching. As representative materials, some metal oxides (e.g. *h*-$MoO_3$) are nonlayered structure which cannot be selectively etched from any parent precursors. In this context, topochemical transformation from a layer of metal precursor to 2D metal oxide is a suitable solution. These new 2D metal oxides can be further topochemically transformed to various 2D metal nitrides and carbides. In addition to metal oxides, metal carbides and sulfides can be also used as the precursors to topochemically create new 2D materials. For topochemical transformation, the choice of precursor and synthesis conditions should be considered thoroughly. For example, $Ti_3C_2$ MXene cannot not be completely transformed to $Ti_3N_2$ even at very high temperature. Instead, $Ti_3CN$ is formed, which we believe is due to the relatively low formation energy of $Ti_3CN$ MXenes. However, this is also a hint that topochemical transformation could be used to synthesize some new carbonitrides and similar compounds, which may also provide novel and useful properties.

We have no doubt that the family of 2D materials will be further expanding with the rapid developments of these topochemical synthesis methods. Significantly, before synthesis of certain 2D materials, one should first check the possible precursors, no matter topochemical deintercalation or transformation. Theoretical calculations and modeling are highly suggested to predict topochemical synthesis feasibility of one precursor to the target material and guide experiments. This can pave a way for one to choose a precursor that is best suited for synthesis instead of performing trials and error tests of numerous precursors. By combining these methods, another interesting direction will be to synthesize 2D materials with the same elements but different stoichiometries (e.g. $Ti_2C$, $Ti_3C_2$, $Ti_4C_3$ and other $Ti_nC_{n-1}$ MXenes, and 2D MoN and $Mo_2N$) or materials with different metals but of the same stoichiometries, such as $Mo_2C$, $Mo_2N$, $W_2C$ and $W_2N$. Numerous solid solutions in oxide, carbide, nitride and other systems should be explored, as they offer possibilities for fine-tuning properties. Finally, synthesis of 2D matrials with separate layers of different elements (similar to $Mo_2TiC_2$ or $Mo_2Ti_2C_3$) that do not exist as bulk material and only possible as 2D materials should be explored. Further research should be

geared towards studying fundamental effects of these parameters on the properties of 2D materials, and further towards fabricating nanodevices.

**Acknowledgements**

We thank Ms. Kathleen Maleski from Drexel University for helpful discussion. H. W. thanks the financial support from the China Scholarship Council (no. 201706920081). P. U. and Y. G. were supported by the U.S. National Science Foundation under grant number DMR-1740795.

**References**:

1. A. K. Geim and K. S. Novoselov, *Nat. Mater.*, 2007, **6**, 183-191.
2. J. N. Coleman, M. Lotya, A. O'Neill, S. D. Bergin, P. J. King, U. Khan, K. Young, A. Gaucher, S. De, R. J. Smith, I. V. Shvets, S. K. Arora, G. Stanton, H.-Y. Kim, K. Lee, G. T. Kim, G. S. Duesberg, T. Hallam, J. J. Boland, J. J. Wang, J. F. Donegan, J. C. Grunlan, G. Moriarty, A. Shmeliov, R. J. Nicholls, J. M. Perkins, E. M. Grieveson, K. Theuwissen, D. W. McComb, P. D. Nellist and V. Nicolosi, *Science*, 2011, **331**, 568-571.
3. V. Nicolosi, M. Chhowalla, M. G. Kanatzidis, M. S. Strano and J. N. Coleman, *Science*, 2013, **340**, 1226419.
4. X. Xu, Z. Zhang, L. Qiu, J. Zhuang, L. Zhang, H. Wang, C. Liao, H. Song, R. Qiao, P. Gao, Z. Hu, L. Liao, Z. Liao, D. Yu, E. Wang, F. Ding, H. Peng and K. Liu, *Nat. Nanotech.*, 2016, **11**, 930-935.
5. C. Xu, L. Wang, Z. Liu, L. Chen, J. Guo, N. Kang, X.-L. Ma, H.-M. Cheng and W. Ren, *Nat. Mater.*, 2015, **14**, 1135-1141.
6. K. R. Paton, E. Varrla, C. Backes, R. J. Smith, U. Khan, A. O'Neill, C. Boland, M. Lotya, O. M. Istrate, P. King, T. Higgins, S. Barwich, P. May, P. Puczkarski, I. Ahmed, M. Moebius, H. Pettersson, E. Long, J. Coelho, S. E. O'Brien, E. K. McGuire, B. M. Sanchez, G. S. Duesberg, N. McEvoy, T. J. Pennycook, C. Downing, A. Crossley, V. Nicolosi and J. N. Coleman, *Nat. Mater.*, 2014, **13**, 624-630.
7. M. Naguib, M. Kurtoglu, V. Presser, J. Lu, J. J. Niu, M. Heon, L. Hultman, Y. Gogotsi and M. W. Barsoum, *Adv. Mater.*, 2011, **23**, 4248-4253.
8. M. Ghidiu, M. Naguib, C. Shi, O. Mashtalir, L. M. Pan, B. Zhang, J. Yang, Y. Gogotsi, S. J. L. Billing and M. W. Barsoum, *Chem. Commun.*, 2014, **50**, 9517-9520.
9. M. Naguib, O. Mashtalir, J. Carle, V. Presser, J. Lu, L. Hultman, Y. Gogotsi and M. W. Barsoum, *ACS Nano*, 2012, **6**, 1322-1331.
10. A. Acun, L. Zhang, P. Bampoulis, M. Farmanbar, A. v. Houselt, A. N. Rudenko, M. Lingenfelder, G. Brocks, B. Poelsema, M. I. Katsnelson and H. J. W. Zandvliet, *J. Phys. Condens. Matter*, 2015, **27**, 443002.
11. E. Bianco, S. Butler, S. Jiang, O. D. Restrepo, W. Windl and J. E. Goldberger, *ACS Nano*, 2013, **7**, 4414-4421.
12. J. R. Dahn, B. M. Way, E. Fuller and J. S. Tse, *Physical Review B*, 1993, **48**, 17872-17877.
13. S. Jiang, S. Butler, E. Bianco, O. D. Restrepo, W. Windl and J. E. Goldberger, *Nat. Commun.*, 2014, **5**, 3389.

14. A. Mustapha Ait and T. Mohamed Rachid, *J. Phys.: Conf. Ser.*, 2014, **491**, 012009.
15. H. Nakano, M. Ishii and H. Nakamura, *Chem. Commun.*, 2005, **0**, 2945-2947.
16. H. Nakano, T. Mitsuoka, M. Harada, K. Horibuchi, H. Nozaki, N. Takahashi, T. Nonaka, Y. Seno and H. Nakamura, *Angew. Chem. Int. Ed.*, 2006, **45**, 6303-6306.
17. E. Noguchi, K. Sugawara, R. Yaokawa, T. Hitosugi, H. Nakano and T. Takahashi, *Adv. Mater.*, 2015, **27**, 856-860.
18. S. M. Pratik, A. Nijamudheen and A. Datta, *Chem. –Eur. J.*, 2015, **21**, 18454-18460.
19. Y. Sugiyama, H. Okamoto, T. Mitsuoka, T. Morikawa, K. Nakanishi, T. Ohta and H. Nakano, *J. Am. Chem. Soc.*, 2010, **132**, 5946-5947.
20. K. Takeda and K. Shiraishi, *Phys. Rev. B*, 1994, **50**, 14916-14922.
21. C. J. Heard, J. Čejka, M. Opanasenko, P. Nachtigall, G. Centi, S. Perathoner, Adv. Mater., 2018, DOI: 10.1002/adma.201801712.
22. X. Xiao, H. Song, S. Lin, Y. Zhou, X. Zhan, Z. Hu, Q. Zhang, J. Sun, B. Yang, T. Li, L. Jiao, J. Zhou, J. Tang and Y. Gogotsi, *Nat. Commun.*, 2016, **7**, 11296.
23. J. Jeon, Y. Park, S. Choi, J. Lee, S. S. Lim, B. H. Lee, Y. J. Song, J. H. Cho, Y. H. Jang and S. Lee, *ACS Nano*, 2018, **12**, 338-346.
24. P. Urbankowski, B. Anasori, K. Hantanasirisakul, L. Yang, L. Zhang, B. Haines, S. May, S. J. L. Billinge and Y. Gogotsi, *Nanoscale*, 2017, **9**, 17722-17730.
25. B. Anasori, M. R. Lukatskaya and Y. Gogotsi, *Nat. Rev. Mater.*, 2017, **2**, 16098.
26. M. Naguib, J. Come, B. Dyatkin, V. Presser, P.-L. Taberna, P. Simon, M. W. Barsoum and Y. Gogotsi, *Electrochem. Commun.*, 2012, **16**, 61-64.
27. A. N. Enyashin and A. L. Ivanovskii, *J. Solid State Chem.*, 2013, **207**, 42-48.
28. A. N. Enyashin and A. L. Ivanoyskii, *J. Phys. Chem. C*, 2013, **117**, 13637-13643.
29. M. Naguib, V. N. Mochalin, M. W. Barsoum and Y. Gogotsi, *Adv. Mater.*, 2014, **26**, 992-1005.
30. B. Anasori, Y. Xie, M. Beidaghi, J. Lu, B. C. Hosler, L. Hultman, P. R. C. Kent, Y. Gogotsi and M. W. Barsoum, *ACS Nano*, 2015, **9**, 9507-9516.
31. Q. Tao, M. Dahlqvist, J. Lu, S. Kota, R. Meshkian, J. Halim, J. Palisaitis, L. Hultman, M. W. Barsoum, P. O. A. Persson and J. Rosen, *Nat. Commun.*, 2017, **8**, 14949.
32. M. Khazaei, A. Ranjbar, M. Arai and S. Yunoki, *Phys. Rev. B*, 2016, **94**, 125152.
33. J. He, P. Lyu and P. Nachtigall, *J. Mater. Chem. C*, 2016, **4**, 2518-2526.
34. W. Sun, Y. Li, B. Wang, X. Jiang, M. Katsnelson, P. A. Korzhavyi, O. Eriksson and I. D. Di Marco, *Nanoscale*, 2016, **8**, 15753-15762.
35. G. Wang, *J. Phys. Chem. C*, 2016, **120**, 18850-18857.
36. T. L. Tan, H. M. Jin, M. B. Sullivan, B. Anasori and Y. Gogotsi, *ACS Nano*, 2017, **11**, 4407−4418.
37. M. Alhabeb, K. Maleski, B. Anasori, P. Lelyukh, L. Clark, S. Sin and Y. Gogotsi, *Chem. Mater.*, 2017, **29**, 7633-7644.
38. O. Mashtalir, M. Naguib, B. Dyatkin, Y. Gogotsi and M. W. Barsoum, *Mater. Chem. Phys.*, 2013, **139**, 147-152.
39. S. Kumar and U. Schwingenschlögl, *Phys. Rev. B*, 2016, **94**, 035405.
40. F. Li, C. R. Cabrera, J. Wang and Z. Chen, *RSC Adv.*, 2016, **6**, 81591-81596.
41. J. Luo, W. Zhang, H. Yuan, C. Jin, L. Zhang, H. Huang, C. Liang, Y. Xia, J. Zhang, Y. Gan and X. Tao, *ACS Nano*, 2017, **11**, 2459-2469.
42. W. Bao, X. Xie, J. Xu, X. Guo, J. Song, W. Wu, D. Su and G. Wang, *Chem. Eur. J.*, 2017, **23**, 12613-12619.

43. M.-Q. Zhao, M. Torelli, C. E. Ren, M. Ghidiu, Z. Ling, B. Anasori, M. W. Barsoum and Y. Gogotsi, *Nano Energy*, 2016, **30**, 603-613.
44. M. R. Lukatskaya, O. Mashtalir, C. E. Ren, Y. Dall'Agnese, P. Rozier, P. L. Taberna, M. Naguib, P. Simon, M. W. Barsoum and Y. Gogotsi, *Science*, 2013, **341**, 1502-1505.
45. M. R. Lukatskaya, S. Kota, Z. Lin, M.-Q. Zhao, N. Shpigel, M. D. Levi, J. Halim, P.-L. Taberna, M. W. Barsoum, P. Simon and Y. Gogotsi, *Nat. Energy*, 2017, **6**, 17105.
46. M. Ghidiu, M. R. Lukatskaya, M. Q. Zhao, Y. Gogotsi and M. W. Barsoum, *Nature*, 2014, **516**, 78-81.
47. C. J. Zhang, B. Anasori, A. Seral-Ascaso, S.-H. Park, N. McEvoy, A. Shmeliov, G. S. Duesberg, J. N. Coleman, Y. Gogotsi and V. Nicolosi, *Adv. Mater.*, 2017, **29**, 1702678.
48. O. Mashtalir, M. R. Lukatskaya, M. Q. Zhao, M. W. Barsoum and Y. Gogotsi, *Adv. Mater.*, 2015, **27**, 3501-3506.
49. M. R. Lukatskaya, S.-M. Bak, X. Yu, X.-Q. Yang, M. W. Barsoum and Y. Gogotsi, *Adv. Energy Mater.*, 2015, **5**, 1500589.
50. Z. W. Seh, K. D. Fredrickson, B. Anasori, J. Kibsgaard, A. L. Strickler, M. R. Lukatskaya, Y. Gogotsi, T. F. Jaramillo and A. Vojvodic, *ACS Energy Lett.*, 2016, **1**, 589-594.
51. G. Gao, A. P. O'Mullane and A. Du, *ACS Catal.*, 2017, **7**, 494-500.
52. R. Li, L. Zhang, L. Shi and P. Wang, *ACS Nano*, 2017, **11**, 3752-3759.
53. P. Srimuk, J. Halim, J. Lee, Q. Tao, J. Rosen and V. Presser, *ACS Sustainable Chem. Eng.*, 2018, **6**, 3739–3747.
54. M. Han, X. Yin, H. Wu, Z. Hou, C. Song, X. Li, L. Zhang and L. Cheng, *ACS Appl. Mater. Interfaces*, 2016, **8**, 21011–21019.
55. R. Sun, H.-B. Zhang, J. Liu, X. Xie, R. Yang, Y. Li, S. Hong and Z.-Z. Yu, *Adv. Funct. Mater.*, 2017, **27**, 1702807.
56. F. Shahzad, M. Alhabeb, C. B. Hatter, B. Anasori, S. M. Hong, C. M. Koo and Y. Gogotsi, *Science*, 2016, **353**, 1137-1140.
57. K. Hantanasirisakul, M.-Q. Zhao, P. Urbankowski, J. Halim, B. Anasori, S. Kota, C. E. Ren, M. W. Barsoum and Y. Gogotsi, *Adv. Electron. Mater.*, 2016, **2**, 1600050.
58. A. D. Dillon, M. J. Ghidiu, A. L. Krick, J. Griggs, S. J. May, Y. Gogotsi, M. W. Barsoum and A. T. Fafarman, *Adv. Funct. Mater.*, 2016, **26**, 4162-4168.
59. J. Halim, M. R. Lukatskaya, K. M. Cook, J. Lu, C. R. Smith, L. A. Naslund, S. J. May, L. Hultman, Y. Gogotsi, P. Eklund and M. W. Barsoum, *Chem. Mater.*, 2014, **26**, 2374-2381.
60. Y. Yang, S. Umrao, S. Lai and S. Lee, *J. Phys. Chem. Lett.*, 2017, **8**, 859-865.
61. K. V. Mahesh, R. Rashada, M. Kiran, A. Peer Mohamed and S. Ananthakumar, *RSC Adv.*, 2015, **5**, 51242-51247.
62. M. Naguib and Y. Gogotsi, *Acc. Chem. Res.*, 2015, **48**, 128-135.
63. M. Alhabeb, K. Maleski, T. S. Mathis, A. Sarycheva, C. B. Hatter, S. Uzun, A. Levitt and Y. Gogotsi, *Angew. Chem. Int. Ed.*, 2018, **130**, 5542-5546.
64. G. Z. Cambaz, G. N. Yushin, Y. Gogotsi and V. G. Lutsenko, *Nano Lett.*, 2006, **6**, 548-551.
65. A. Lipatov, M. Alhabeb, M. R. Lukatskaya, A. Boson, Y. Gogotsi and A. Sinitskii, *Adv. Electron. Mater.*, 2016, **2**, 1600255.
66. L. H. Karlsson, J. Birch, J. Halim, M. W. Barsoum and P. O. Persson, *Nano Lett.*, 2015, **15**, 4955-4960.

67. P. Urbankowski, B. Anasori, T. Makaryan, D. Er, S. Kota, P. L. Walsh, M. Zhao, V. B. Shenoy, M. W. Barsoum and Y. Gogotsi, *Nanoscale*, 2016, **8**, 11385-11391.
68. R. Meshkian, L.-Å. Näslund, J. Halim, J. Lu, M. W. Barsoum and J. Rosen, *Scripta Mater.*, 2015, **108**, 147-150.
69. J. Halim, S. Kota, M. R. Lukatskaya, M. Naguib, M.-Q. Zhao, E. J. Moon, J. Pitock, J. Nanda, S. J. May, Y. Gogotsi and M. W. Barsoum, *Adv. Funct. Mater.*, 2016, **26**, 3118-3127.
70. J. Zhou, X. Zha, F. Y. Chen, Q. Ye, P. Eklund, S. Du and Q. Huang, *Angew. Chem.*, 2016, **128**, 5092-5097.
71. T. M. Gesing and W. Jeitschko, *J. Solid State Chem.*, 1998, **140**, 396-401.
72. O. Mashtalir, M. Naguib, V. N. Mochalin, Y. Dall'Agnese, M. Heon, M. W. Barsoum and Y. Gogotsi, *Nat. Commun.*, 2013, **4**, 1716.
73. K. Maleski, V. N. Mochalin and Y. Gogotsi, *Chem. Mater.*, 2017, **29**, 1632-1640.
74. R. Ma and T. Sasaki, *Acc. Chem. Res.*, 2015, **48**, 136-143.
75. J. Xuan, Z. Wang, Y. Chen, D. Liang, L. Cheng, X. Yang, Z. Liu, R. Ma, T. Sasaki, and F. Geng, *Angew. Chem.*, 2016, **128**, 14789-14794.
76. M. Naguib, R. R. Unocic, B. L. Armstrong and J. Nanda, *Dalton T.*, 2015, **44**, 9353-9358.
77. N. C. Osti, M. Naguib, A. Ostadhossein, Y. Xie, P. R. Kent, B. Dyatkin, G. Rother, W. T. Heller, A. C. van Duin, Y. Gogotsi and E. Mamontov, *ACS Appl. Mater. Interfaces*, 2016, **8**, 8859-8863.
78. N. Shpigel, M. R. Lukatskaya, S. Sigalov, C. E. Ren, P. Nayak, M. D. Levi, L. Daikhin, D. Aurbach and Y. Gogotsi, *ACS Energy Lett.*, 2017, **2**, 1407-1415.
79. S.-M. Bak, R. Qiao, W. Yang, S. Lee, X. Yu, B. Anasori, H. Lee, Y. Gogotsi and X.-Q. Yang, *Adv. Energy Mater.*, 2017, **7**, 1700959.
80. A. H. Feng, Y. Yu, F. Jiang, Y. Wang, L. Mi, Y. Yu and L. X. Song, *Ceram. Int.*, 2017, **43**, 6322-6328.
81. O. Mashtalir, K. M. Cook, V. N. Mochalin, M. Crowe, M. W. Barsoum and Y. Gogotsi, *J. Mater. Chem. A,* 2014*,* **2**, 14334–14338.
82. C. E. Ren, K. B. Hatzell, M. Alhabeb, Z. Ling, K. A. Mahmoud and Y. Gogotsi, *J. Phys. Chem. Lett.*, 2015, **6**, 4026-4031.
83. K. Maleski, C. E. Ren, M.-Q. Zhao, B. Anasori and Y. Gogotsi, *ACS Appl. Mater. Interfaces*, 2018, **10**, 24491-24498.
84. E. Bonitz, *Chem. Ber.*, 1961, **94**, 220-225.
85. Y.G. Gogotsi, J.-D. Jeon and M.J. McNallan, *J. Mater. Chem.*, 1997, **7**, 1841-1848.
86. M. R. Tchalala1, M. A. Ali, H. Enriquez, A. Kara, A. Lachgar, S. Yagoubi, E. Foy, E. Vega, A. Bendounan, and M. G. Silly, *J. Phys.: Condens. Matter*, 2013, **25**, 442001.
87. R. Raccichini, A. Varzi, S. Passerini, and B. Scrosati, *Nat. Mater.*, 2015, **14**, 271-279.
88. F. Bonaccorso, L. Colombo, G. Yu, M. Stoller, V. Tozzini, A. C. Ferrari, R. S. Ruoff, and V. Pellegrini, *Science*, 2015, **347**, 1246501.
89. Y. Park, B. Ryu, B.-R. Oh, Y. Song, X. Liang, and K. Kurabayashi, *ACS Nano*, 2017, **11**, 5697-5705.
90. T. F. Jaramillo, K. P. Jørgensen, J. Bonde, J. H. Nielsen, S. Horch, and I. Chorkendorff, *Science*, 2007, **317**, 100-102.
91. F. Wang, Z. Wang, T. A. Shifa, Y. Wen, F. Wang, X. Zhan, Q. Wang, K. Xu, Y. Huang, L. Yin, C. Jiang, and J. He, *Adv. Funct. Mater.*, 2017, **27**, 1603254.

92. V. Nicolosi, M. Chhowalla, M. G. Kanatzidis, M. S. Strano, and J. N. Coleman, *Science*, 2013, **340**, 1420–1438.
93. D. Hanlon, C. Backes, T. M. Higgins, M. Hughes, A. O'Neill, P. King, N. McEvoy, G. S. Duesberg, B. M. Sanchez, H. Pettersson, V. Nicolosi and J. N. Coleman, *Chem. Mater.*, 2014, **26**, 1751–1763.
94. W. C. Lee, K. Kim, J. Park, J. Koo, H. Y. Jeong, H. Lee, D. A. Weitz, A. Zettl and S. T. Lee, *Nat. Nanotechnol.*, 2015, **10**, 423–428.
95. L. Zheng, Y. Xu, D. Jin and Y. Xie, *Chem. Mater.*, 2009, **21**, 5681–5690.
96. M. Xu, T. Liang, M. Shi and H. Chen, *Chem. Rev.*, 2013, **113**, 3766–3798.
97. A. Zavabeti, J. Z. Ou, B. J. Carey, N. Syed, R. Orrell-Trigg, E. L. H. Mayes, C. Xu, O. Kavehei, A. P. O'Mullane, R. B. Kaner, K. Kalantar-zadeh and T. Daeneke, *Science*, 2017, **358**, 332-335.
98. D. Chandler, J. D. Weeks and H. C. Andersen, *Science*, 1983, **220**, 787–794.
99. B. J. Carey, J. Z. Ou, R. M. Clark, K. J. Berean, A. Zavabeti, A. S. R. Chesman, S. P. Russo, D. W. M. Lau, Z.-Q. Xu, Q. Bao, O. Kavehei, B. C. Gibson, M. D. Dickey, R. B. Kaner, T. Daeneke and K. Kalantar-Zadeh, *Nat. Commun.*, 2017, **8**, 14482.
100. N. Syed, A. Zavabeti, J. Z. Ou, M. Mohiuddin, N. Pillai, B. J. Carey, B. Y. Zhang, R. S. Datta, A. Jannat, F. Haque, K. A. Messalea, C. Xu, S. P, Russo, C. F. McConville, T. Daeneke and K. Kalantar-Zadeh, *Nat. Commun.*, 2018, **9**, 3618.
101. T. Daenke, P. Atkin, R. Orrell-Trigg, A. Zavabeti, T. Ahmed, S. Walia, M. Liu, Y. Tachibana, M. Javaid, A. D. Greentree, S. P. Russo, R. B. Kaner and K. Kalantar-Zadeh, *ACS Nano*, 2017, **11**, 10974-10983.
102. J. Zhu, Z. Yin, H. Li, H. Tan, C. L. Chow, H. Zhang, H. H. Hng, J. Ma and Q. Yan, *Small*, 2011, **7**, 3458-3464.
103. S. Takenaka, S. Miyake, S. Uwai, H. Matsune and M. Kishida, *J. Phys. Chem. C*, 2015, **119**, 12445-12454.
104. H. Cao, X. Zhou, C. Zheng, Z. Liu, *ACS Appl. Mater. Interfaces*, 2015, **7**, 11984-11990.
105. Z. Li, X. Y. Yu, U. Paik, *J. Power Sources*, 2016, **310**, 41-46.
106. W. Eom, A. Kim, H. Park, H. Kim, T. H. Han, *Adv. Funct. Mater.*, 2016, **26**, 7605-7613.
107. W. Cheng, J. He, T. Yao, Z. Sun, Y. Jiang, Q. Liu, S. Jiang, F. Hu, Z. Xie, B. He, W. Yan, and S. Wei, *J. Am. Chem. Soc.*, 2014, **136**, 10393−10398.
108. Z. Hu, X. Xiao, H. Jin, T. Li, M. Chen, Z. Liang, Z. Guo, J. Li, J.Wan, L. Huang, Y.Zhang, G. Feng and J. Zhou, *Nat. Commun.*, 2017, **8**, 15630.
109. A. K. Sinha, M. Pradhan, and T. Pal, *J. Phys. Chem. C*, 2013, **117**, 23976–23986.
110. J. F. Xie, S. Li, X. D. Zhang, J. J. Zhang, R. X. Wang, H. Zhang, B. C. Pan and Y. Xie, *Chem. Sci.*, 2014, **5**, 4615−4620.
111. Z. Y. Al Balushi, K. Wang, R. K. Ghoshe, R. A. Vila, S. M. Eithfeld, J. D. Caldwell, X. Y. Qin, Y. C. Lin, P. A. DeSario, G. Stone, S. Subremanian, D. F. Paul, R. M. Wallace, S. Datta, J. M. Redwing and J. A. Robinson, *Nat. Mater.*, 2016, **15**, 1166−1171.
112. J. N. Coleman, M. Lotya, A. O'Neill1, S. D. Bergin, P. J. King, U. Khan, K. Young, A. Gaucher, S. De, R. J. Smith, I. V. Shvets, S. K. Arora, G. Stanton, H.-Y. Kim, K. Lee, G. T. Kim, G. S. Duesberg, T. Hallam, J. J. Boland, J. J.Wang, J. F. Donegan, J. C. Grunlan, G. Moriarty, A. Shmeliov, R. J. Nicholls, J. M. Perkins, E. M. Grieveson, K. Theuwissen, D. W. McComb, P. D. Nellist and V. Nicolosi, *Science*, 2011, **331**, 568−571.
113. K. R. Paton, E. Varrla, C. Backes, R. J. Smith, U. Khan, A. O'Neill, C. Boland, M. Lotya, O. M. Istrate, P. King, T. Higgins, S. Barwich, P. May, P. Puczkarski, I. Ahmed,

M. Moebius, H. Pettersson, E.Long, J. Coelho, S. E. O'Brien, E. K. McGuire, B. M. Sanchez, G. S. Duesberg, N. McEvoy, T. J. Pennycook, C. Downing, A. Crossley, V. Nicolosi and J. N. Coleman, *Nat. Mater.*, 2014, **13**, 624−630.
114. X. Xiao, H. Yu, H. Jin, M. Wu, Y. Fang, J. Sun, Z. Hu, T. Li, J. Wu, L. Huang, Y. Gogotsi and J. Zhou, *ACS Nano*, 2017, **11**, 2180−2186.
115. J. Xiong, W. Cai, W. Shi, X. Zhang, J. Li, Z. Yang, L. Feng and H. Cheng, *J. Mater. Chem. A*, 2017, **5**, 24193-24198.
116. J. Xiong, J. Li, J. Shi, X. Zhang, N.-T. Suen, Z. Liu, Y. Huang, G. Xu, W. Cai, X. Lei, L. Feng, Z. Yang, L. Huang and H. Cheng, *ACS Energy Lett.*, 2018, **3**, 341-348.
117. S. K. Balakrishnan and P. V. Kamat, *Chem. Mater.*, 2018, **30**, 74-78.
118. R. Ma, Z. Liu, K. Takada, N. Lyi, Y. Bando and T. Sasaki, *J. Am. Chem. Soc.*, 2007, **129**, 5257-5263.
119. D. Lu, D. J. Baek, S. S. Hong, L. F. Kourkoutis, Y. Hikita and H. Y. Hwang, *Nat. Mater.*, 2016, **15**, 1255-1260.
120. L. Kavan, M. Kalbáč, M. Zukalová, I. Exnar, V. Lorenzen, R. Nesper and M. Graetzel, *Chem. Mater.*, 2004, **16**, 477-485.
121. R. S. Datta, J. Z. Ou, M. Mohiuddin, B. J. Carey, B. Y. Zhang, H. Khan, N. Syed, A. Zavabeti, F. Haque, T. Daeneke and K. Kalantar-Zadeh, *Nano Energy*, 2018, **49**, 237-246.
122. P. Chen, K. Xu, X. Li, Y. Guo, D. Zhou, J. Zhao, X. Wu, C. Wu and Y. Xie, *Chem. Sci.*, 2014, **5**, 2251-2255.
123. Y. Zhu, C. Cao, S. Tao, W. Chu, Z. Wu and Y. Li, *Sci. Rep.*, 2014, **4**, 5787.
124. M. Baghbanzadeh, L. Carbone, P. D. Cozzoli and C. O. Kappe, *Angew. Chem. Int. Ed.*, 2011, **50**, 11312–11359.
125. J. Feng, X. Sun, C. Wu, L. Peng, C. Lin, S. Hu, J. Yang and Y. Xie, *J. Am. Chem. Soc.*, 2011, **133**, 17832–17838.
126. H. Wu, X. Lu, G. Zheng, and G. W. Ho, *Adv. Energy Mater.*, 2018, **8**, 1702704.
127. X. Lu, G. Wang, T. Zhai, M. Yu, S. Xie, Y. Ling, C. Liang, Y. Tong and Y. Li, *Nano Lett.*, 2012, **12**, 5376-5381.
128. K. Xu, P. Chen, X. Li, Y. Tong, H. Ding, X. Wu, W. Chu, Z. Peng, C. Wu and Y. Xie, *J. Am. Chem. Soc.*, 2015, **137**, 4119-4125.
129. F. Xie, T. Liu, L. Xie, X. Sun and Y. Luo, *Sensors Actuat. B-Chem.*, 2018, **255**, 2794-2799.
130. J. Jia, T. Xiong, L. Zhao, F. Wang, H. Liu, R. Hu, J. Zhou, W Zhou and S. Chen, *ACS Nano*, 2017, **11**, 12509-12518.
131. B. Soundiraraju and B. K. George, *ACS Nano*, 2017, **11**, 8892-8900.
132. I. Shein and A. Ivanovskii, *Comp. Mater. Sci.*, 2012, **65**, 104-114.
133. P. Urbankowski, B. Anasori, K. Hantanasirisakul, L. Yang, L. Zhang, B. Haines, S. J. May, S. J. L. Billinge and Y. Gogotsi, *Nanoscale*, 2017, **9**, 17722-17730.
134. Y. Wen, T. E. Rufford, X. Chen, N. Li, M. Lyu, L. Dai and L. Wang, *Nano Energy*, 2017, **38**, 368-376.
135. J. Halim, S. Kota, M. R. Lukatskaya, M. Naguib, M. Q. Zhao, E. J. Moon, J. Pitock, J. Nanda, S. J. May and Y. Gogotsi, *Adv. Funct. Mater.*, 2016, **26**, 3118-3127.
136. K. D. Fredrickson, B. Anasori, Z. W. Seh, Y. Gogotsi and A. Vojvodic, *J. Phys. Chem. C*, 2016, **120**, 28432-28440.

137. T. Huang, S. Mao, G. Zhou, Z. Wen, X. Huang, S. Ci and J. Chen, *Nanoscale*, 2014, **6**, 9608-9613.
138. X. Zhou, H. Chen, D. Shu, C. He and J. Nan, *J. Phys. Chem. solid.*, 2009, **70**, 495-500.
139. Y. Zhong, X. Xia, F. Shi, J. Zhan, J. Tu and H. Fan, *Adv. Sci.*, 2016, **3**, 1500286.
140. J. Jeon, Y. Park, S. Choi, J. Lee, S. S. Lim, B. H. Lee, Y. J. Song, J. H. Cho, Y. H. Jang and S. Lee, *ACS Nano*, 2018, **12**, 338-346.
141. Y. Wang and Y. Ding, *J. Mater. Chem. C*, 2018, **6**, 2245-2251.
142. N. Li, X. Chen, W.-J. Ong, D. R. MacFarlane, X. Zhao, A. K. Cheetham and C. Sun, *ACS Nano*, 2017, **11**, 10825-10833.
143. S. Ghasemi, M. H. Abbasi, A. Saidi, J. Y. Kim and J. S. Lee, *Ind. Eng. Chem. Res.*, 2011, **50**, 13340-13346.
144. D. H. Youn, S. Han, J. Y. Kim, J. Y. Kim, H. Park, S. H. Choi and J. S. Lee, *ACS Nano*, 2014, **8**, 5164-5173.
145. U. Yorulmaz, A. Özden, N. K. Perkgöz, F. Ay and C. Sevik, *Nanotechnology*, 2016, **27**, 335702.
146. H. P. Hughes and H. Starnberg, *Electron spectroscopies applied to low-dimensional structures*, Springer Science & Business Media, 2001.
147. M. Sreedhara, K. Vasu and C. Rao, *Z. Anorg. Allg. Chem.*, 2014, **640**, 2737-2741.
148. G. D. Sun, G. H. Zhang and K. C. Chou, *J. Am. Ceram. Soc*., 2018, **101**, 2796-2808.

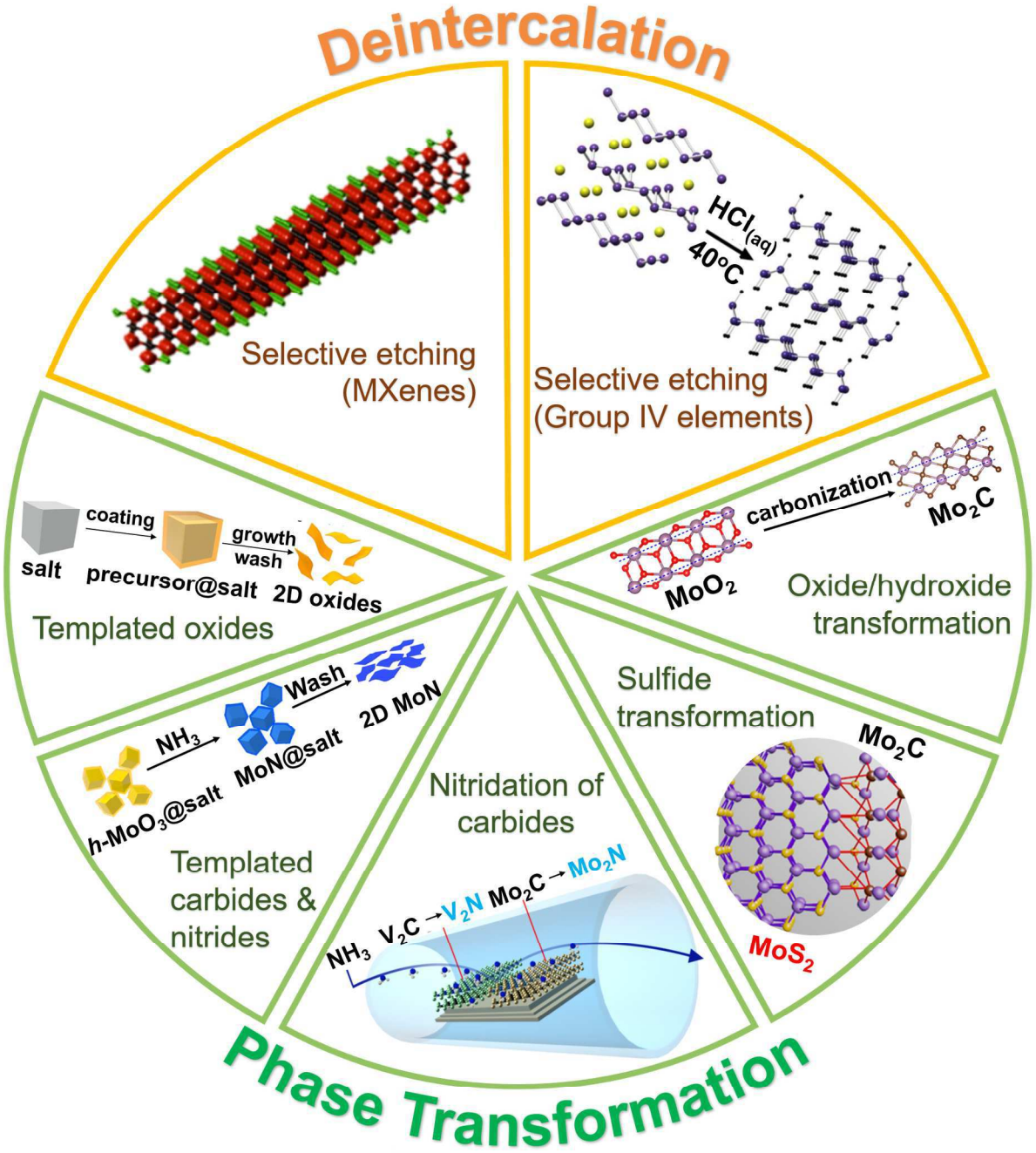


**Fig. 1** Schematic of the variety of topochemical synthesis process as used for making 2D materials, which includes topochemical deintercalation and transformation, such as selective etching of precursors to synthesize MXenes, silicene and germanene; salt-templated synthesis of 2D metal oxides, carbides and nitrides; nitridation of carbide MXenes to produce nitride MXenes; transformation of metal sulfides, oxides and hydroxides to other 2D materials. Separate panels reproduced from ref. 11 with permission from American Chemical Society, ref. 22 with permission from Nature Publishing Group, ref. 114 with permission from American Chemical

Society, ref. 133 with permission from the Royal Society of Chemistry, ref. 23 with permission from American Chemical Society and ref. 130 with permission from American Chemical Society.

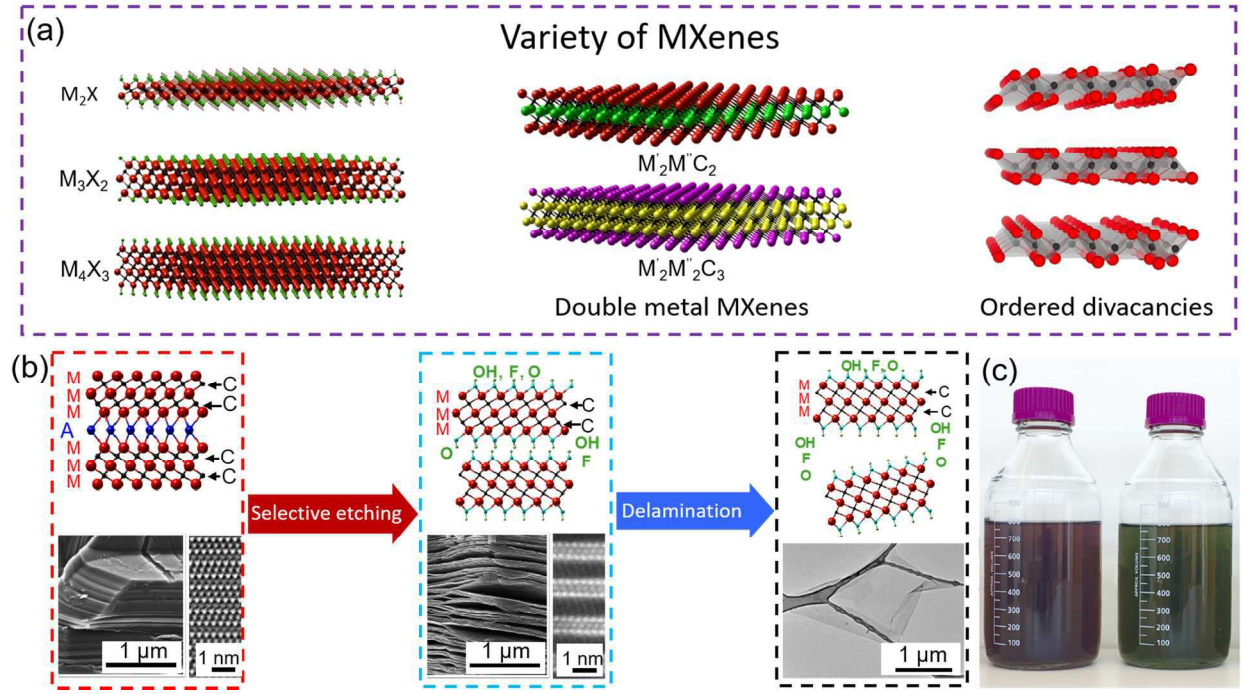


**Fig. 2** (a) Atomic structures show the variety of MXenes. There are single metal MXenes with three stoichiometries ($M_2X$, $M_3X_2$, and $M_4X_3$) as well as double-metal MXenes ($M'_2M''C_2$ and $M'_2M''_2C_3$) and $M_{1.33}C$ with ordered divacancies. Reproduced from ref. 30 with permission from American Chemical Society. Reproduced from ref. 31 with permission from Nature Publishing Group. (b) The synthesis process of MXenes, which includes selective etching of the mono atomic "A" layers and an expansion in the structure as shown by SEM. Etching is followed by delamination of 2D materials into single layers as shown by TEM. Reproduced from ref. 30 with permission from American Chemical Society. (c) Optical image of diluted colloidal solutions of $Ti_2CT_x$ and $Ti_3C_2T_x$ MXene (0.02 mg/mL) in 1 L bottles. Reproduced from ref. 37 with permission from American Chemical Society.

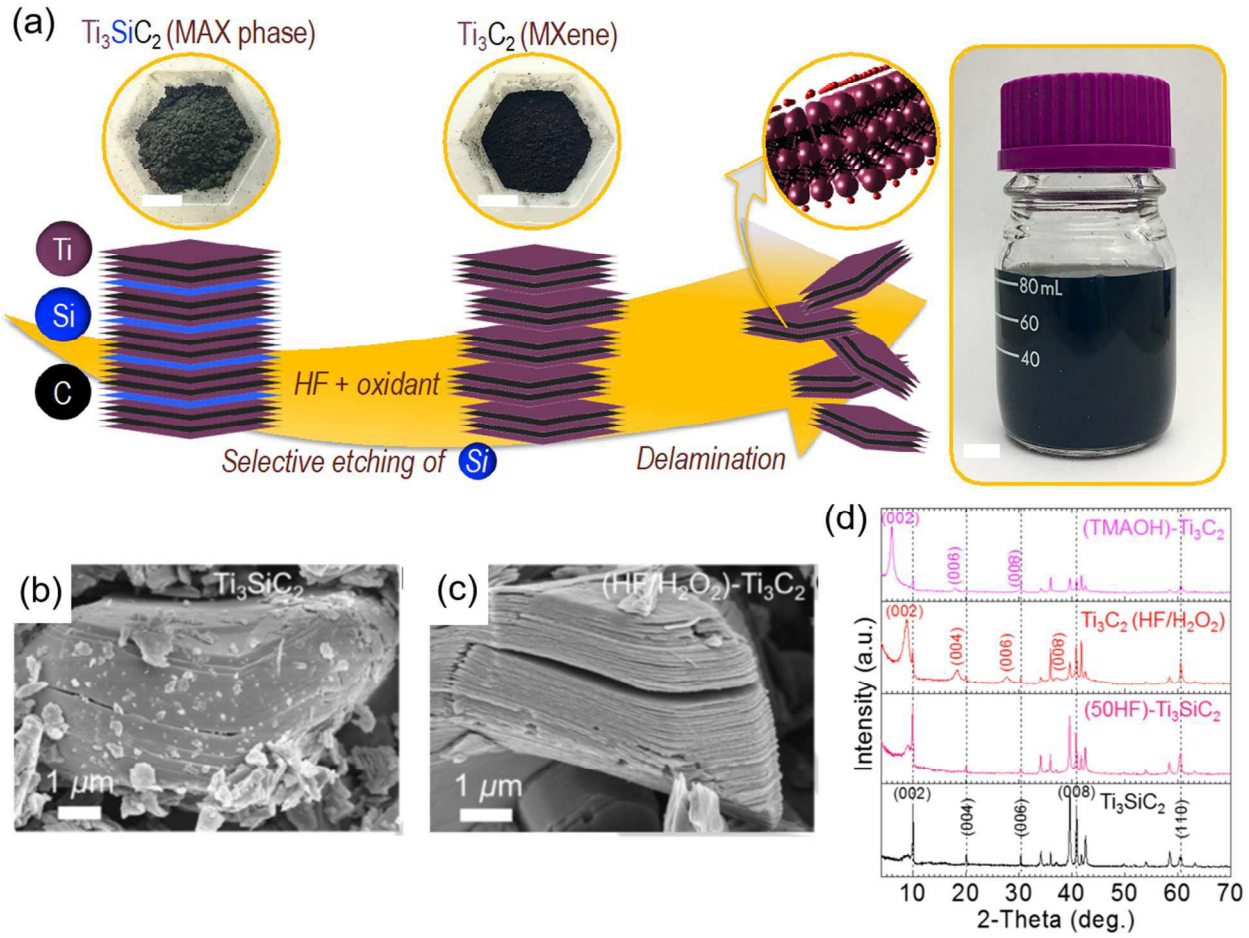


**Fig. 3** (a) Schematic of the synthesis of $Ti_3C_2$ (MXene) from $Ti_3SiC_2$ MAX phase: Si was selectively etched by using an etching solution consisting of HF and an oxidant ($H_2O_2$, $(NH_4)_2S_2O_8$, $HNO_3$, $KMnO_4$ or $FeCl_3$). The color of the precursor MAX powder is gray-to-silver (top left) and the MXene powder is black. A glass vial is shown containing 80 mL of stable colloidal solution of delaminated MXene. All scale bars are 1 cm. (b) SEM image of $Ti_3SiC_2$ MAX phase. (c) SEM image of $Ti_3C_2$ MXene after selective etching by $HF/H_2O_2$. (d) XRD patterns of $Ti_3SiC_2$ MAX phase, 50 wt.% HF etched $Ti_3SiC_2$, $HF/H_2O_2$ etched $Ti_3C_2$ and TMAOH delaminated $Ti_3C_2$ MXene. Reproduced from ref. 63 with permission from Wiley-VCH.

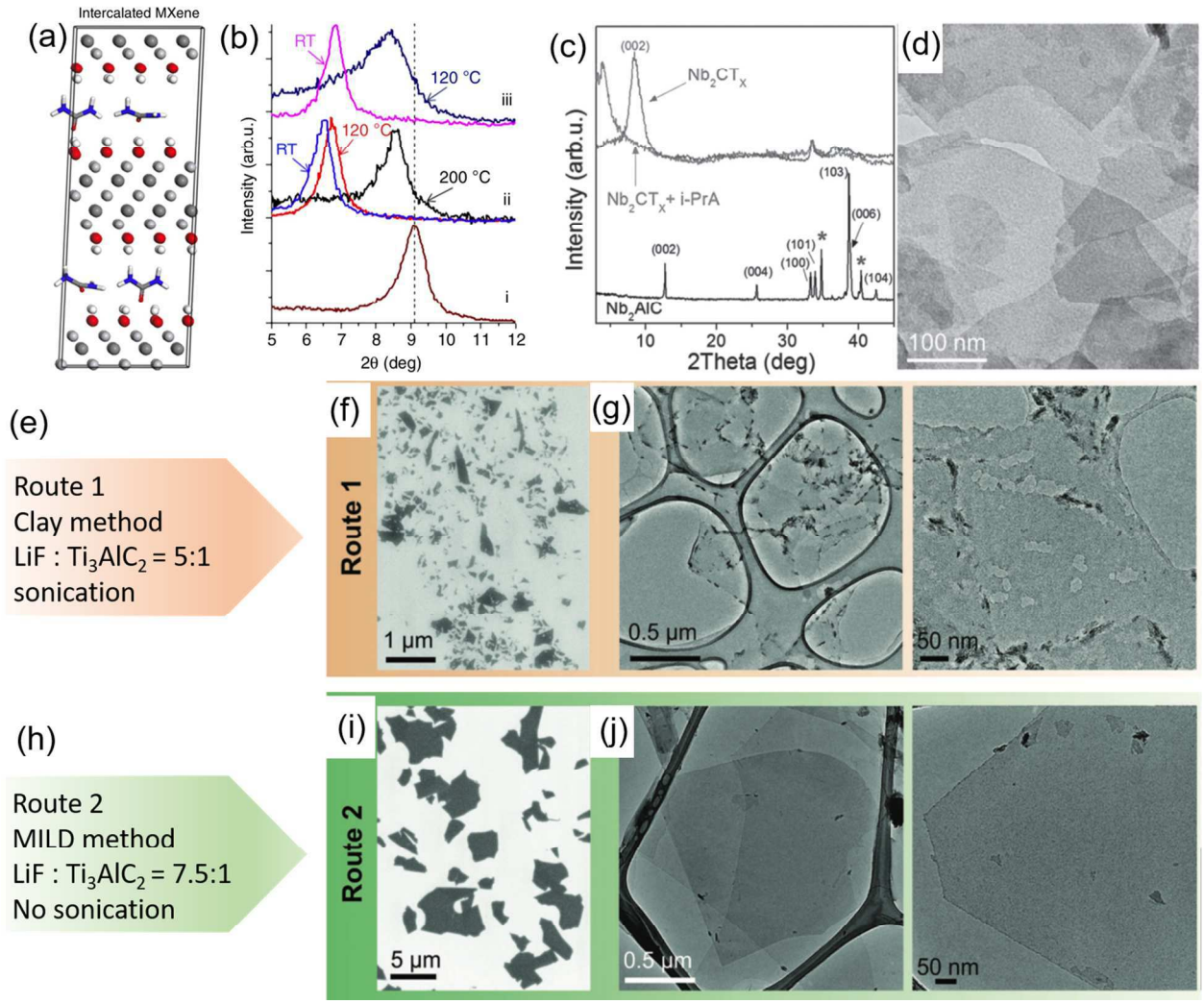


**Fig. 4** (a) Atomic structure of intercalated $M_3X_2T_x$ MXene (urea is shown as an example of intercalant). (b) XRD patterns of as-synthesized $Ti_3C_2$ before intercalation (i), $Ti_3C_2$ after treatment with hydrazine monohydrate (HM) in DMF and dried under different conditions (ii), $Ti_3C_2$ after HM treatment and dried in different conditions (iii). Reproduced from ref. 72 with permission from Nature Publishing Group. (c) XRD patterns of $Nb_2AlC$ powder (bottom), exfoliated $Nb_2CT_x$, and isopropylamine intercalated $Nb_2CT_x$ ($Nb_2CT_x$ + i-PrA). (d) TEM image of delaminated $Nb_2CT_x$ flakes. Reproduced from ref. 48 with permission from Wiley-VCH. (e)-(g) SEM and TEM images of $Ti_3C_2$ flakes produced by "clay" synthesis method. (h)-(j) SEM and TEM images of $Ti_3C_2$ flakes produced by MILD synthesis method. Reproduced from ref. 65 with permission from Wiley-VCH.

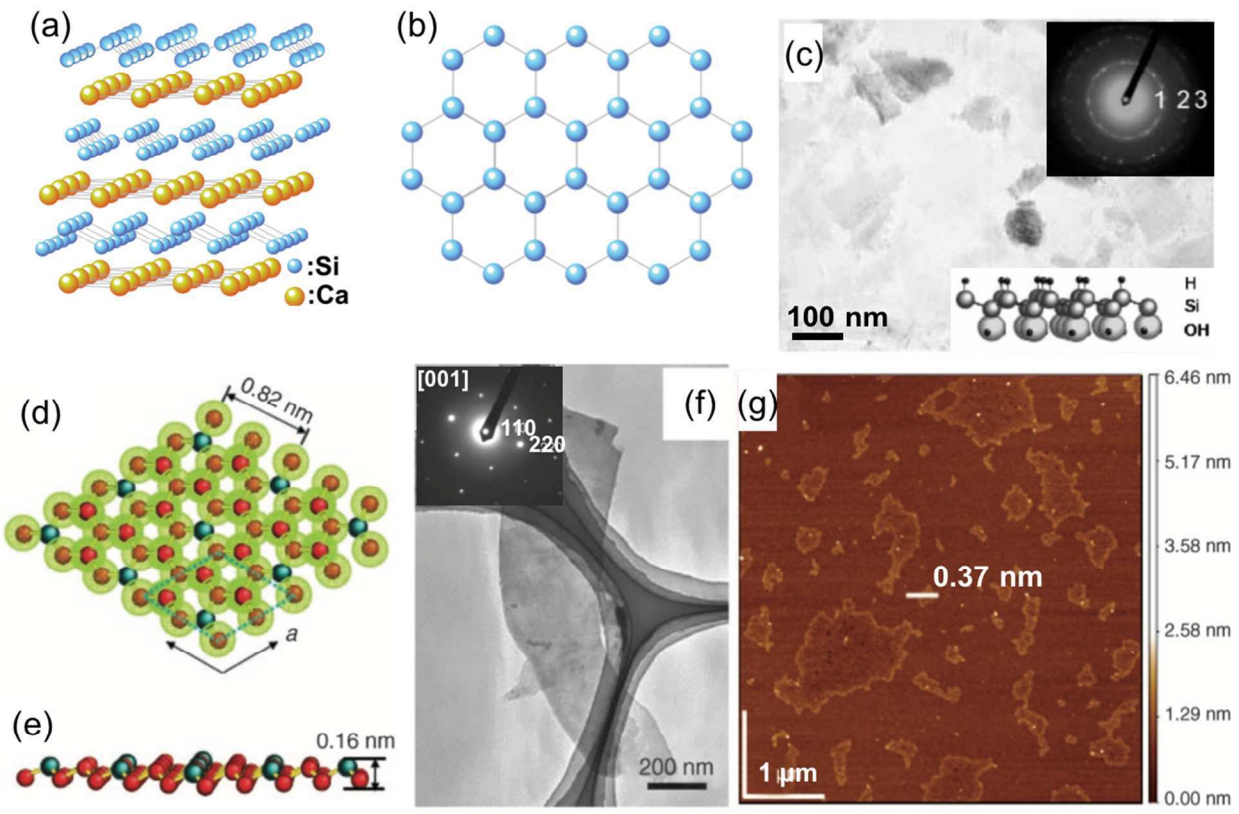


**Fig. 5** (a) Atomic structure of $CaSi_2$. (b) Top view of the atomic structure of silicene layers in $CaSi_2$. Reproduced from ref. 17 with permission from Wiley-VCH. (c) TEM image of siloxene nanosheets. Inset is the electron diffraction pattern (top) and atomic structure of siloxene nanosheets (bottom). Reproduced from ref. 15 with permission from the Royal Society of Chemistry. (d) Top view of $Mg_{1.3}Si_7O_{7.5}$ sheet terminated by oxygen. (e) Side view of the core of the $Mg_{1.3}Si_7O_{7.5}$ sheet; the large yellow-green circles represent oxygen atoms, small red (Si) and green (Mg) circles represent the Si (111) plane in the layer below. (f) TEM image and electron diffraction pattern (inset) of the sheet. (g) AFM image of the $Mg_{1.3}Si_7O_{7.5}$ sheets. Reproduced from ref. 16 with permission from Wiley-VCH.

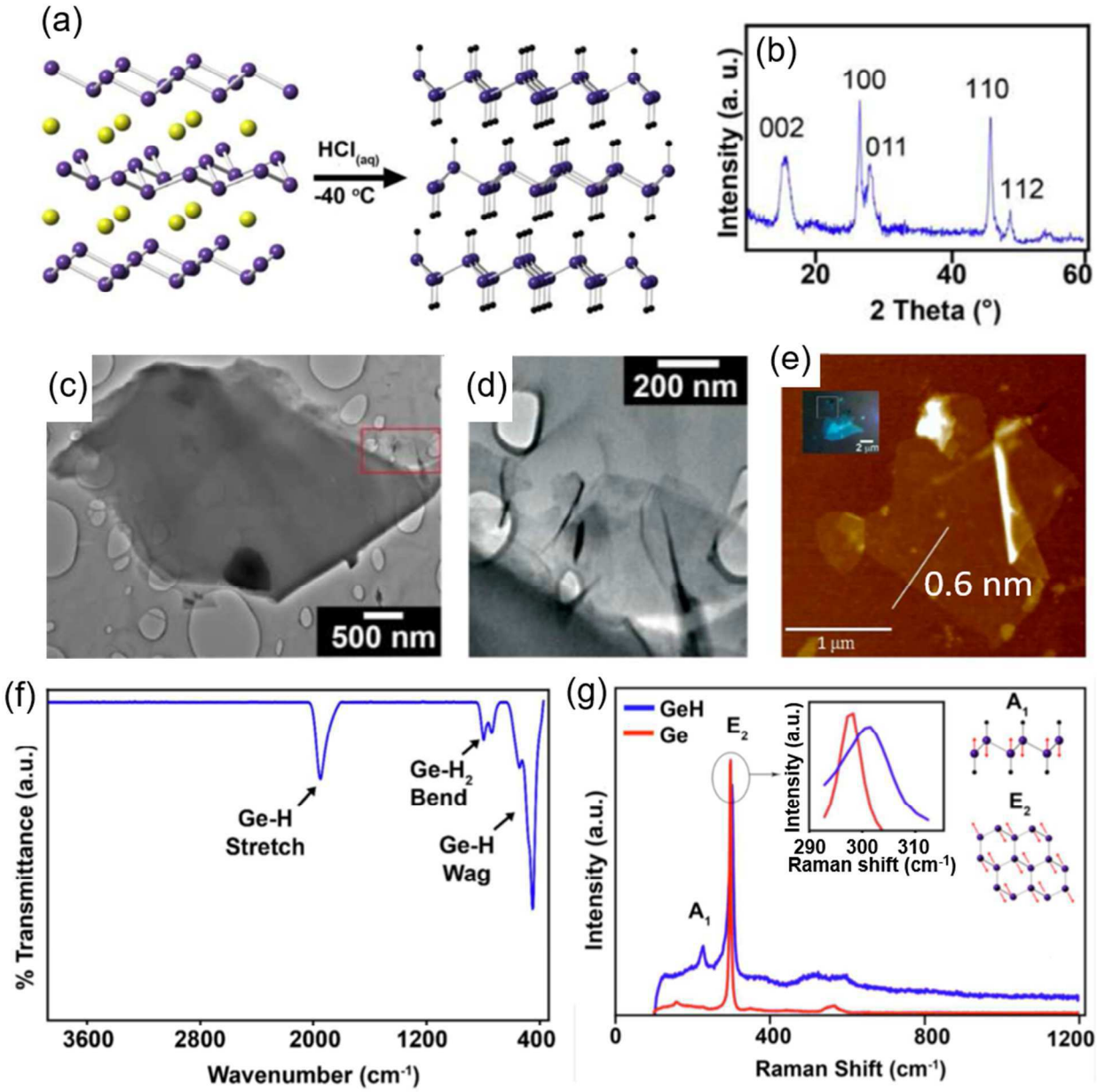


**Fig. 6** (a) Schematic illustration shows the topochemical deintercalation of $CaGe_2$ to form GeH. (b) XRD pattern of GeH. (c) Low-magnification and (d) magnified TEM images of multilayered GeH. (e) AFM micrograph of monolayer GeH sheet. (f) Transmission-mode FTIR of GeH. (g) Raman spectrum of GeH (red) and Ge powder (blue). Reproduced from ref. 11 with permission from American Chemical Society.

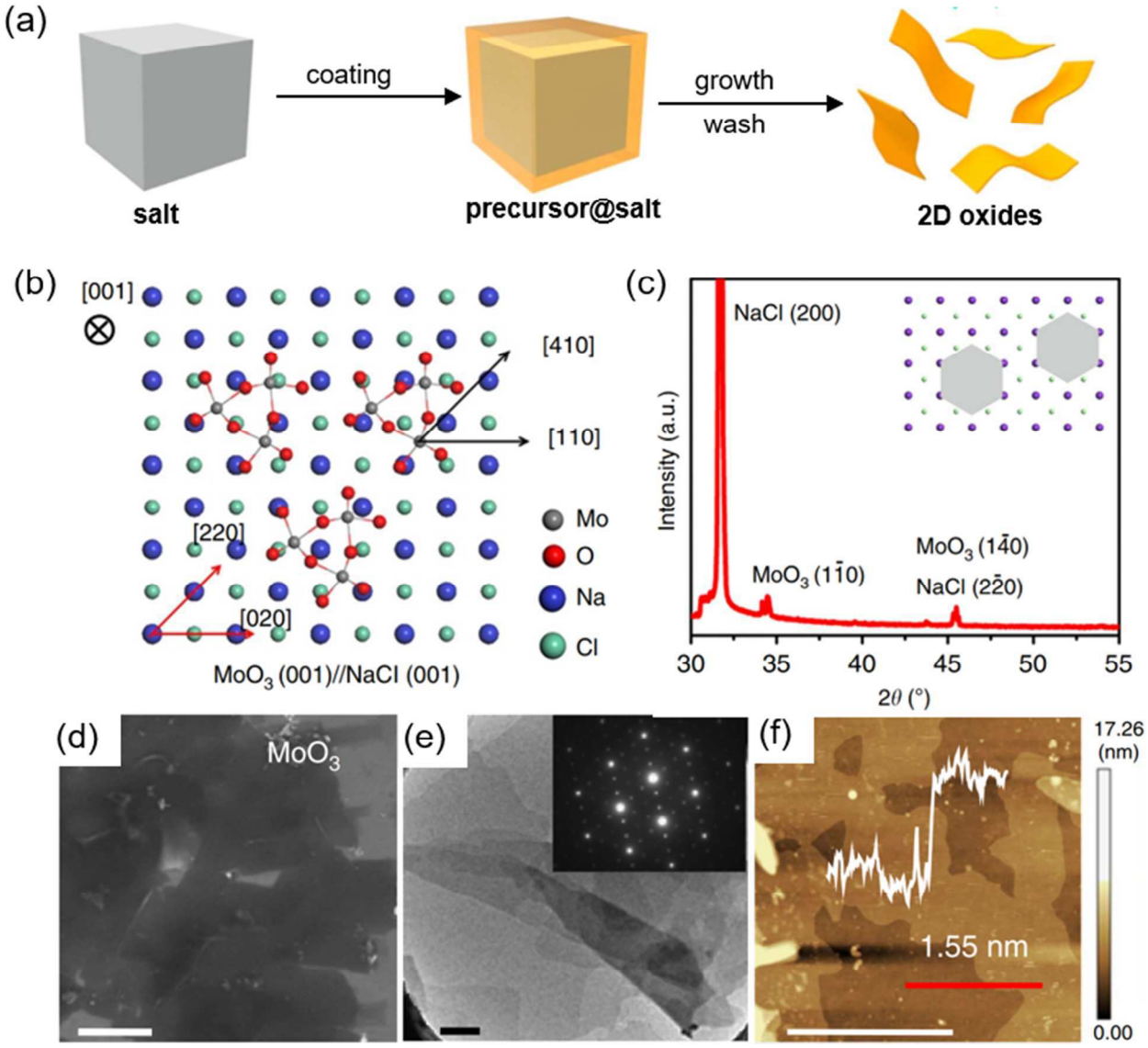


**Fig. 7**. (a) Schematic representation of 2D *h*-$MoO_3$ synthesis. (b) Proposed mechanism of the salt-assisted templated growth of *h*-$MoO_3$. (c) XRD pattern of 2D *h*-$MoO_3$ on NaCl. The inset is a schematic representation of *h*-$MoO_3$ on NaCl. (d) SEM, (e) low-resolution TEM and (f) AFM images of 2D *h*-$MoO_3$ Scale bar: 20 μm (d), 500 nm (e), 1 μm (f). The inset of (e) shows the corresponding selected area electron diffraction (SAED) patterns. The inset of (f) shows the corresponding thickness of the 2D oxide. Scan line is shown in red. Reproduced from ref. 22 with permission from Nature Publishing Group.

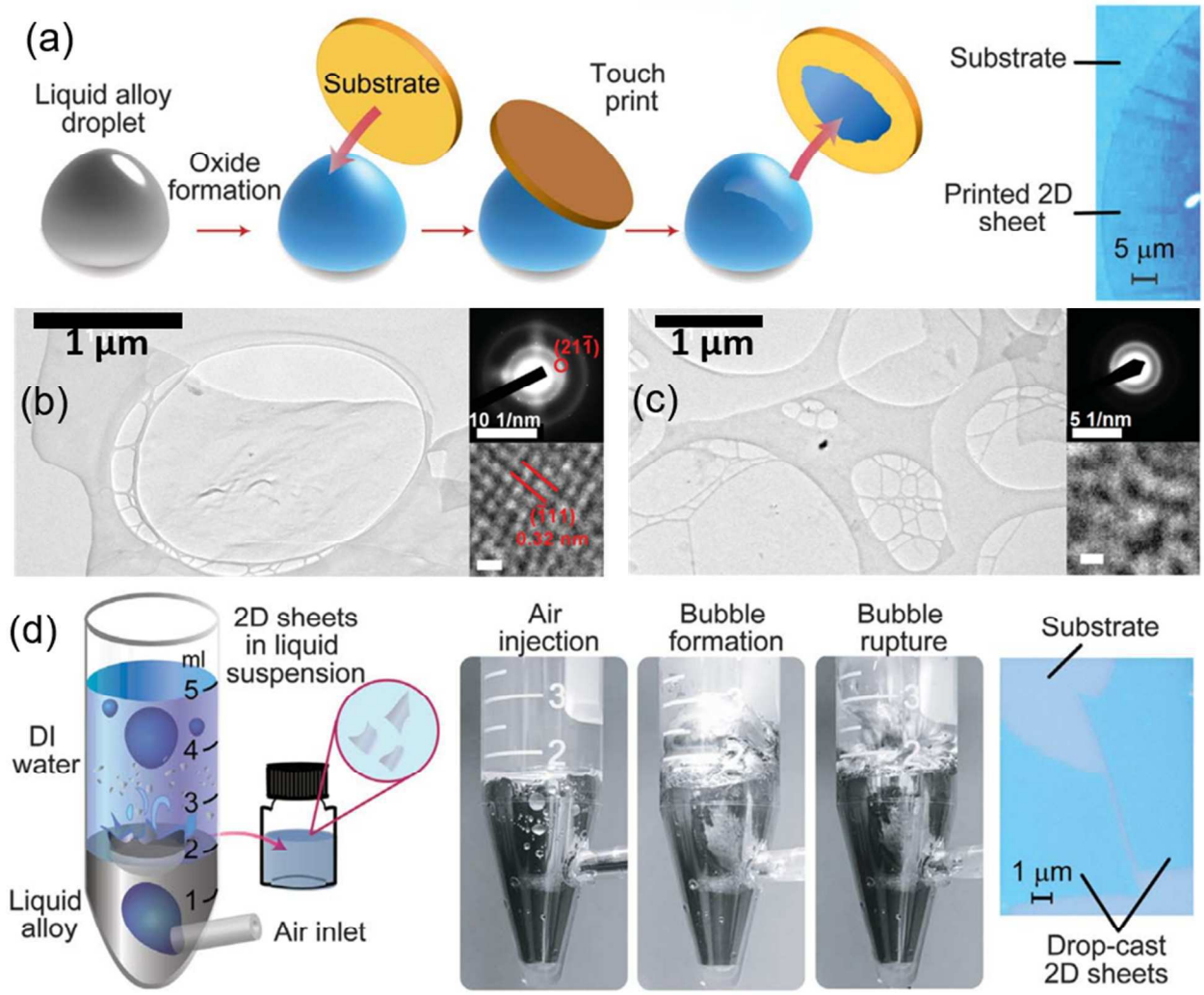


**Fig. 8.** (a) Schematic representation of the oxide-on-metal exfoliation technique. An optical image of the deposited oxide sheet is shown at the right. (b) Characterization of $HfO_2$ derived from the oxide exfoliation method. TEM characterization, with SAED (top inset) and HRTEM images (bottom inset; scale bar, 0.5 nm). (c) Characterization of $HfO_2$ derived from the gas injection method. TEM characterization, with SAED (top inset) and HRTEM images (bottom inset; scale bar, 0.5 nm). (d) Schematic representation of the gas injection method (left), photographs of the bubble bursting through the liquid metal (center), and an optical image of the resulting sheets drop-cast onto a $SiO_2$/Si wafer (right). The eutectic GaInSn alloy is used as a base liquid metal for all alloying and synthesis processes. Reproduced from ref. 97 with permission from American Association for the Advancement of Science.

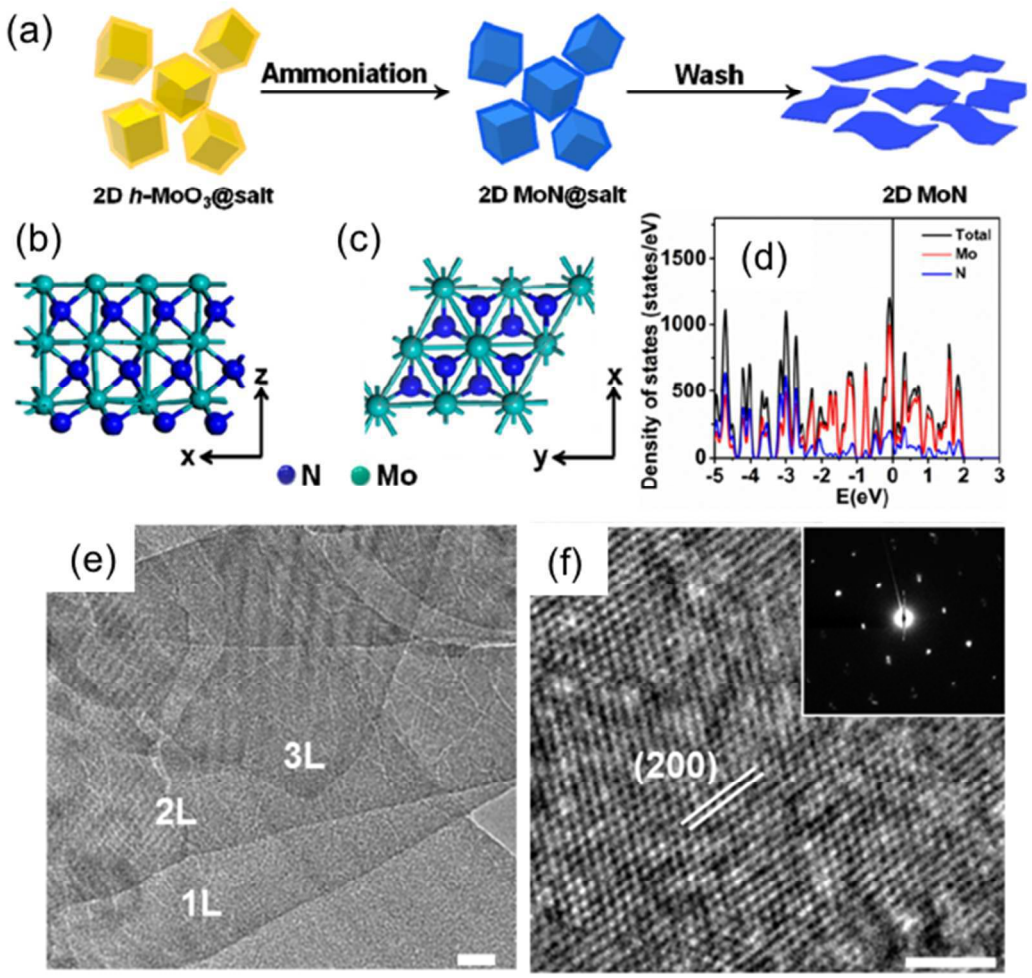


**Fig. 9.** (a) Schematic illustration of 2D MoN synthesis. (b, c) Side and top view images of the atomic structure of 2D MoN. (d) density of states of 2D MoN. (e) TEM image of overlapping single-layer MoN nanosheets. Scale bar, 20 nm. (f) HRTEM shows that 2D MoN is single-crystalline with a hexagonal structure. The inset is a SAED that demonstrates the single-crystal structure of 2D MoN. Scale bar, 2 nm. Reproduced from ref. 114 with permission from American Chemical Society.

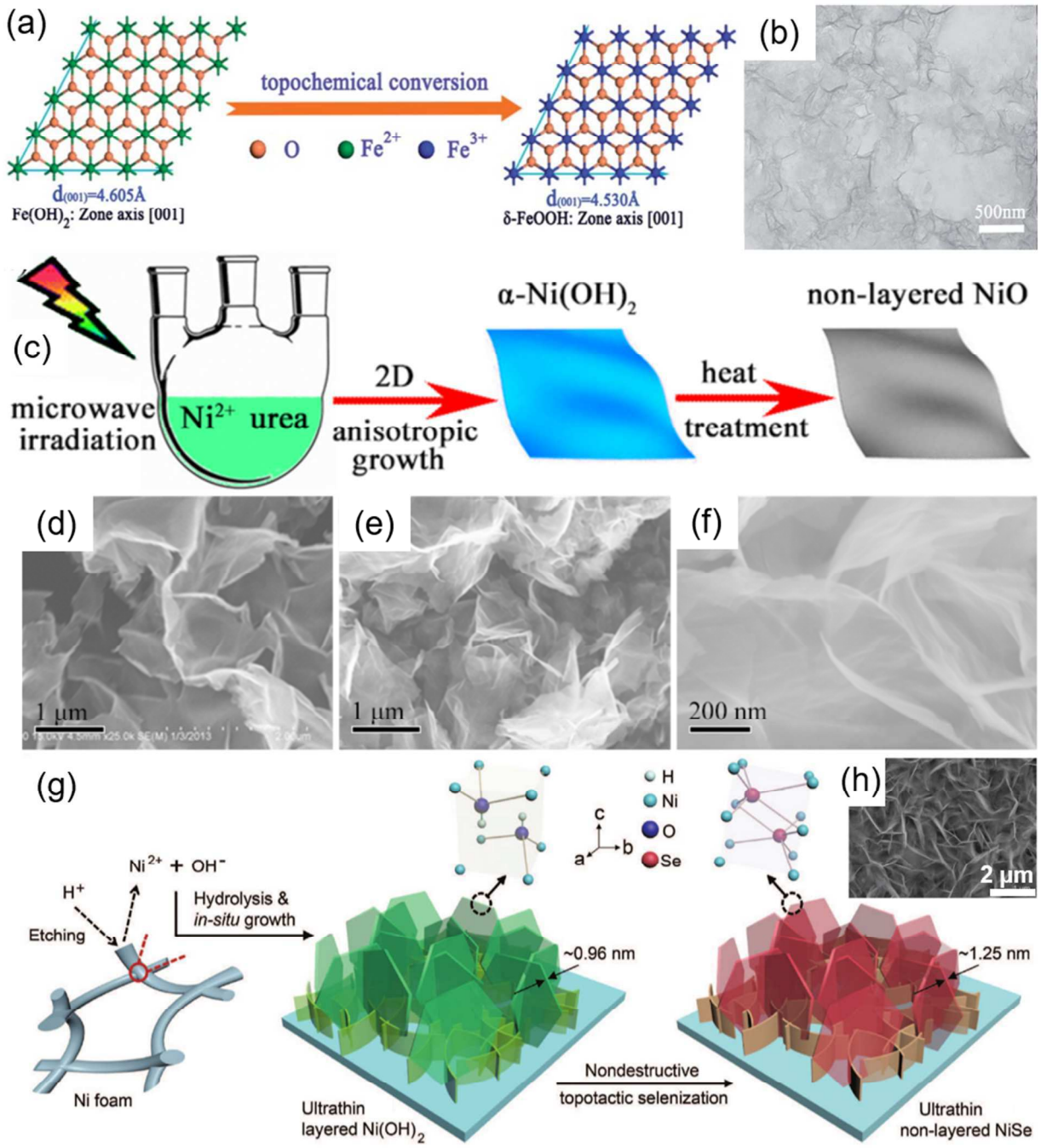


**Fig. 10**. (a) Top-view of the c-axis showing the topochemical conversion from the $Fe(OH)_2$ (001) plane to the *d*-FeOOH (001) plane. (b) TEM image of *d*-FeOOH ultrathin nanosheets. Reproduced from ref. 122 with permission from the Royal Society of Chemistry. (c) Schematic illustrating synthesis of nanosheets; FESEM images of (d) *α*-$Ni(OH)_2$ and (e), (f) NiO nanosheets. Reproduced from ref. 123 with permission from Nature Publishing Group. (g) Structural evolution of ultrathin 2D layered $Ni(OH)_2$ nanosheets and ultrathin 2D non-layered

NiSe nanosheets through combinatorial acid etching and topotactic selenization. (h) SEM image of ultrathin NiSe nanosheets. Reproduced from ref. 126 with permission from Wiley-VCH.

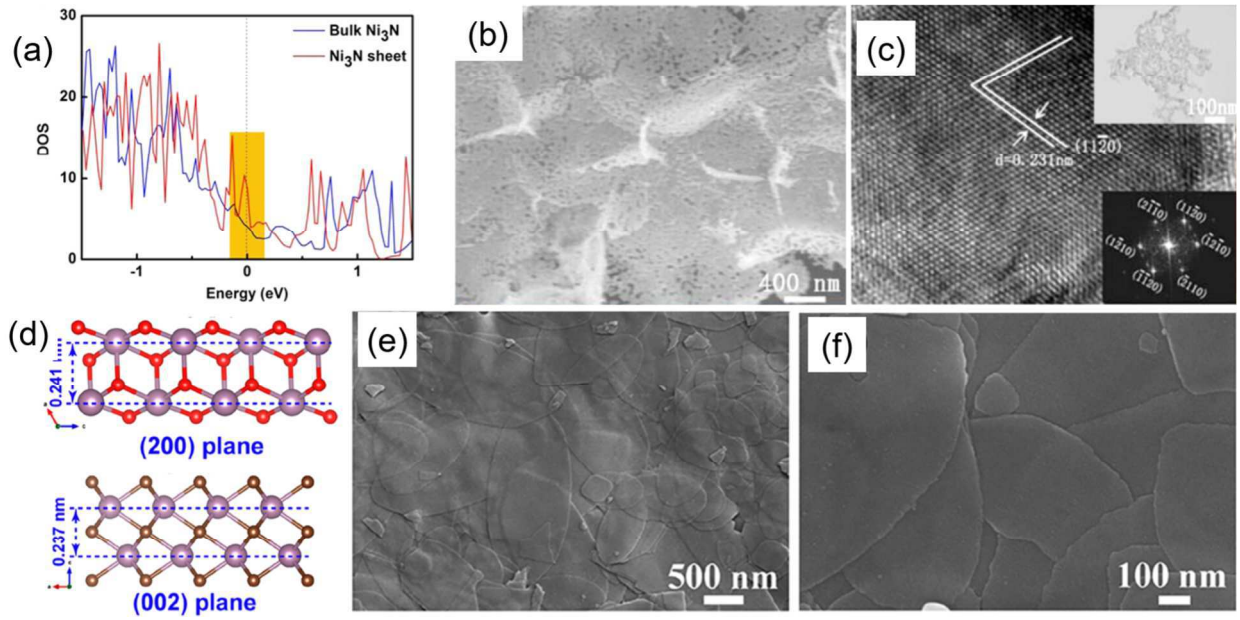


**Fig. 11.** (a) Calculated density of states for bulk $Ni_3N$ and $Ni_3N$ sheet. The Fermi level is set at 0 eV. (b) SEM image and (c) HRTEM image (Inset: corresponding FFT pattern and TEM image) of $Ni_3N$ nanosheets. Reproduced from ref. 128 with permission from American Chemical Society. (d) Crystal models of $MoO_2$ nanosheets (top) and N-$Mo_2C$ nanosheets (bottom). SEM images of (e) $MoO_2$ and (f) N-$Mo_2C$ nanosheets. Reproduced from ref. 130 with permission from American Chemical Society.

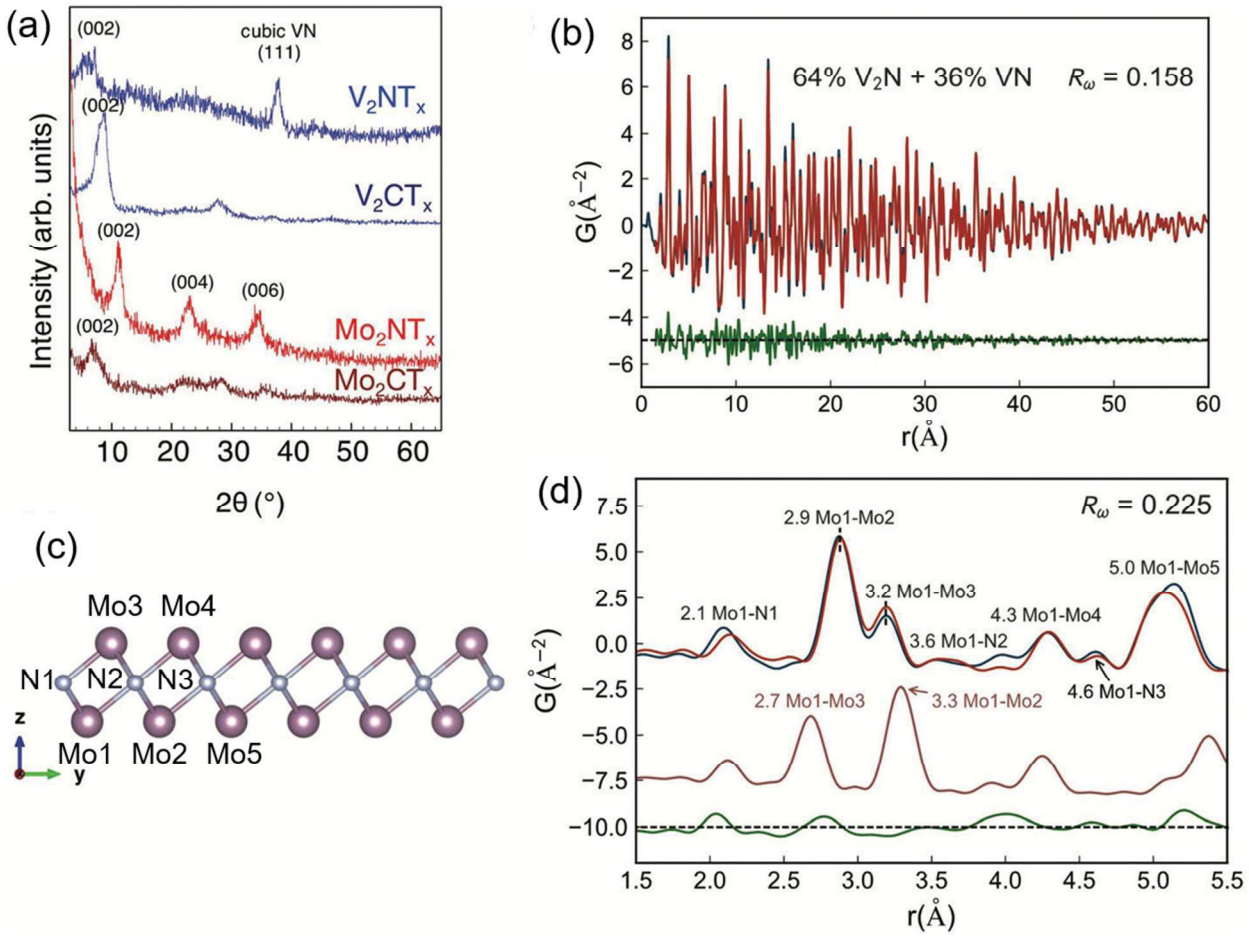


**Fig. 12**. (a) XRD patterns of $Mo_2CT_x$ and $V_2CT_x$ before and after ammoniation for 1 h at 600 °C. $Mo_2NT_x$ produced by the ammoniation of $Mo_2CT_x$ maintained a 2D MXene structure as evidenced by the presence of the (002) peak at 2θ = 11°, which is typical for $M_2X$ MXenes. For the $V_2CT_x$ sample after ammoniation (top blue curve), a broad peak appears at 2θ = 7.0°, and a peak appears at 37°. (b) X-ray pair distribution function (PDF) fit (red curve) of the 64% $V_2N$ + 36% VN (mass ratio) mixed phase model and measured data (blue curve), with difference curve offset in green. $R_\omega$ is goodness of fit (a lower value corresponds to a better fit). (c) Single slab model of $Mo_2N$ after structure refinement, projected along the *x*-axis. (d) PDF fit (red curve on top) of the $Mo_2N$ single slab model after structure refinement to the measured data (top blue curve) with a difference offset (bottom green). Simulated PDF of the initial $Mo_2N$ MXene single slab model (same atomic positions as the precursor $Mo_2C$ MXene structural model) without structure refinement (middle brown) is shown in the offset curve below the measured data (top blue curve). Reproduced from ref. 133 with permission from the Royal Society of Chemistry.

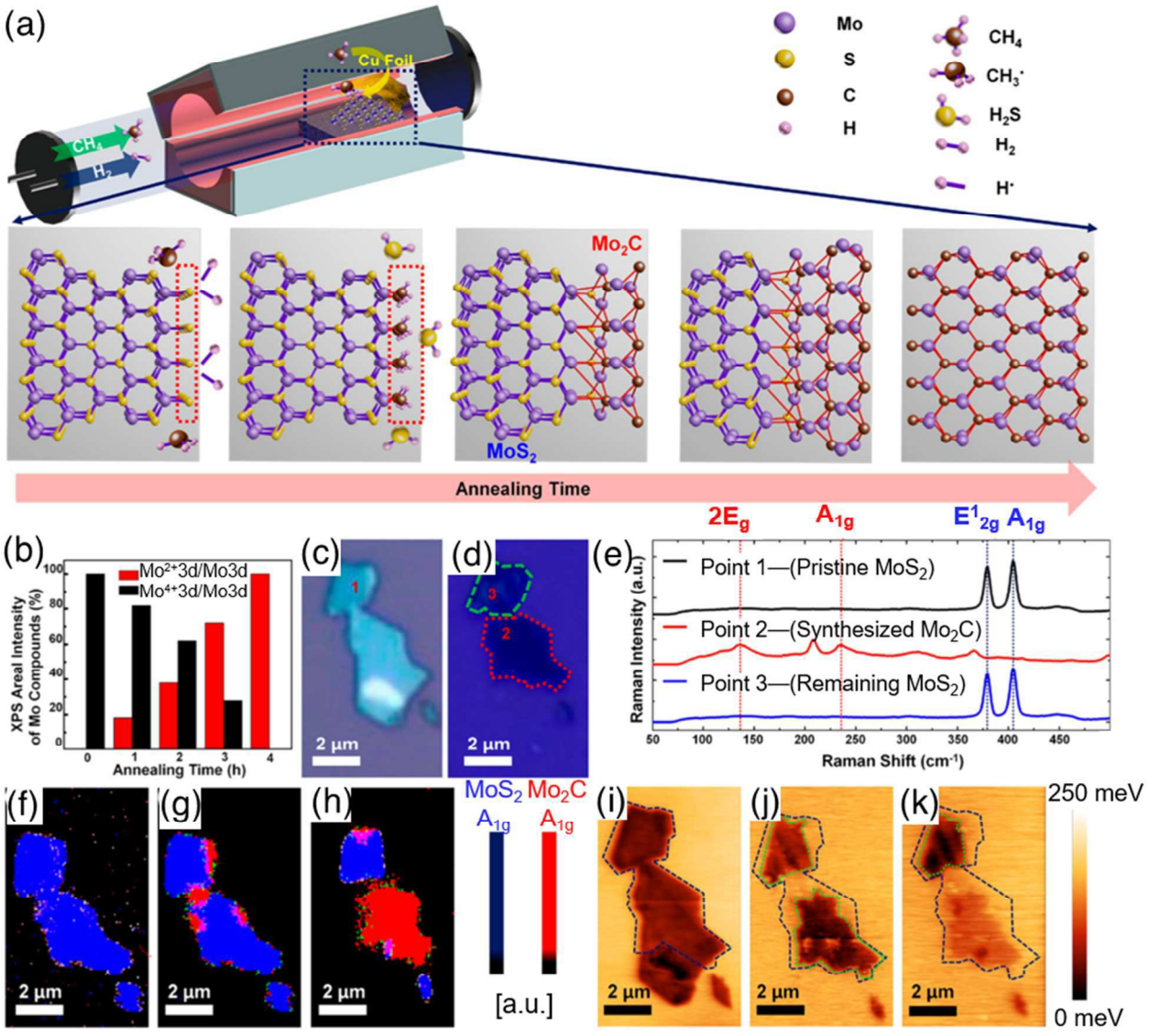


**Fig. 13**. (a) Schematic of $Mo_2C$ synthesis *via* thermal annealing of $MoS_2$ in a $CH_4$ and $H_2$ mixture. (b) XPS statistical analysis of the $Mo_2C/MoS_2$ product to obtain the peak intensity percentages of the total intensity of Mo 3d for components corresponding to $Mo^{4+}$ and $Mo^{2+}$. (c) Optical microscope image of an exfoliated $MoS_2$ flake and (d) Optical microscope image of a flake after partial conversion to $Mo_2C$ over 3 h of thermal annealing. (e) Raman spectra from the points numbered in (c) and (d). Raman mapping image of the $A_{1g}$ modes of $MoS_2$ and $Mo_2C$ before annealing (f), after annealing for 1 h (g), and after annealing for 3 h (h). Work function mapping images extracted from the KPFM measurements obtained before annealing (i), after annealing for 1 h (j), and after 3 h of annealing (k). Reproduced from ref. 23 with permission from American Chemical Society.

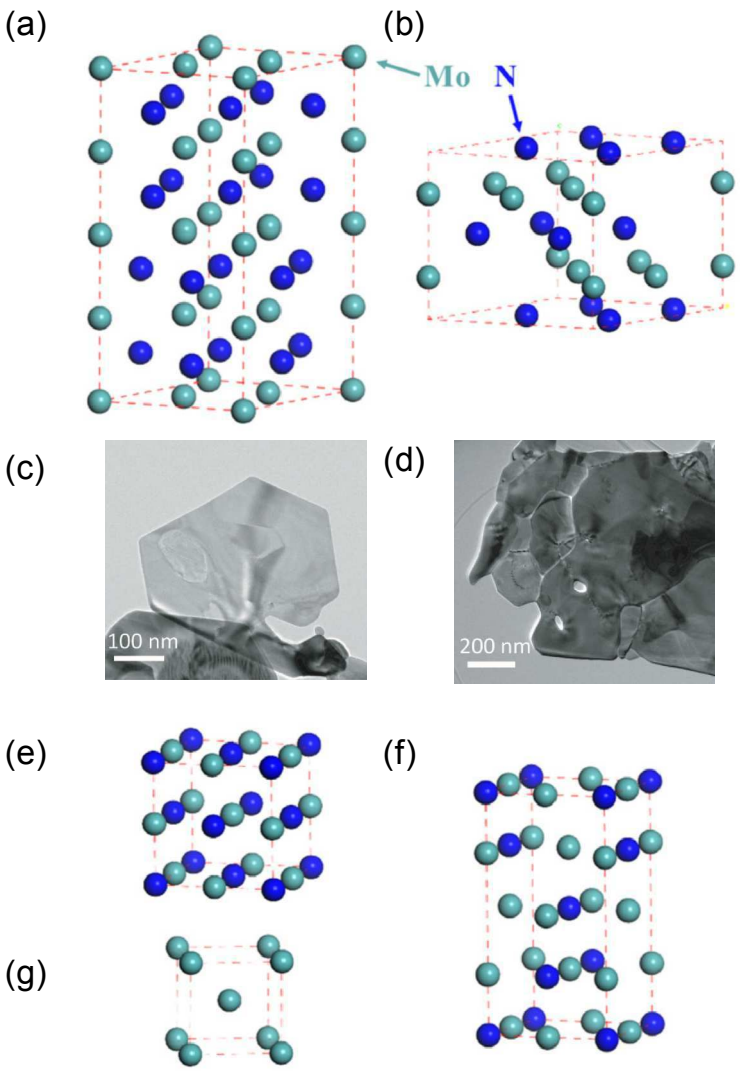


**Fig. 14.** Crystal structures of molybdenum nitrides synthesized by nitridation of 2H-$MoS_2$. (a) $Mo_5N_6$ ($P6_3/m$); (b) δ-MoN ($P6_3mc$); (c) TEM image for $Mo_5N_6$; (d) TEM image for δ-MoN; (e) γ-$Mo_2N$ (Fm-3m); (f) β-$Mo_2N$ ($I4_1/amd$); (g) Mo (Im-3 m). Reproduced from ref. 148 with permission from Wiley-VCH.

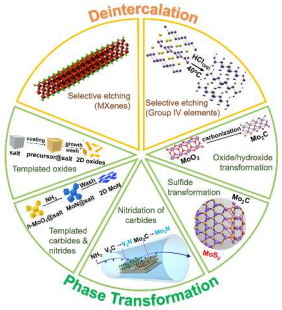


This review summarizes the rapidly-developed topochemical synthesis of 2D materials, explains the growth mechanisms and provides outlooks for future research.